New Journal and we have not received input yet 26 (2021) 101079

Contents lists available at ScienceDirect

Thermal Science and Engineering Progress

journal homepage: www.sciencedirect.com/journal/thermal-science-and-engineering-progress

Cavitation models with thermodynamic effect for organic fluid cavitating flows in organic Rankine cycle systems: A review

Wenguang Li, Zhibin Yu *

School of Engineering, University of Glasgow, Glasgow G12 8QQ, UK

ARTICLE INFO

Keywords:
Cavitation model
Thermodynamic effect
Organic Rankine cycle
Organic fluid
Rayleigh-Plesset equation
Nucleation cavitation model

ABSTRACT

Organic Rankine cycle (ORC) power plants are considered as one of the most promising technologies to generate power from low temperature heat sources such as biomass combustion, industrial waste heat, geothermal heat, and solar thermal energy. A feed pump is a key component of an ORC power plant to circulate the working fluid within the system. Owing to the low boiling temperature of most organic fluids, the feed pumps of ORC power plants are more vulnerable to suffer from cavitation. Cavitation of the organic fluid in the feed pump in an ORC system can degrade the evaporator performance and cause instabilities in the system operation. Properly determining the required net positive suction head or subcooling for the pump is critical for the ORC system design and operation. Thus, this paper presents a systematic review of cavitation models with thermodynamic effect in simulations of cavitating flows. Methods for implementing thermodynamic effect were summarised. The features of the cavitation models were characterised and criticized, and their drawbacks were identified. A number of newly established cavitation models were explained and discussed in detail. Homogeneous mixture cavitation models have advantages such as less computational effort and easier implementation of thermodynamic effect in comparison with fully coupled multiscale models. However, when the thermodynamic effect is considered in the existing cavitation models, the cavitation regimes are not distinguished and applied properly. Nucleation cavitation models for organic fluids in ORC systems should be developed in terms of experimental nuclei profile and non-condensable gas concentration in future.

1. Introduction

The organic Rankine cycle (ORC) is a Rankine cycle that employs an organic fluid as working medium to generate power from lower temperature sources such as biomass combustion, industrial waste heat, and geothermal heat [1–5]. In an ORC system, a feed pump must be used to deliver the organic fluid to the evaporator, as shown in Fig. 1a. Although a laboratory-scale pumpless ORC system was tested [6,7] and thermofluidic feed pumps have been tested in laboratory ORC systems [8,9], mechanical feed pumps are still commonly employed in laboratory- or large-scale ORC systems [10,11] due to their simple constructure and easy operation. The feed pumps used in ORC systems are classified based on delivery method and illustrated in Fig. 1b.

Since an improper mechanical feed pump can impair the performance of the evaporator, and, in turn, the performance of the expander in an ORC system, a number of studies have been conducted on mechanical feed pumps in ORC systems to clarify pump performance and cavitation behaviour when delivering organic fluids. The pumping work in ORC systems was estimated analytically for 18 different organic fluids [12]; it was identified that the feed pump in ORC systems should develop high head (0.2–40 bar) and low mass flow rate (0.01–10 kg/s) [13]. There are currently two types of pumps which can meet these requirements: rotodynamic pumps and positive displacement pumps. The rotodynamic pump employs one or more rotating impellers to raise both liquid pressure and velocity continuously, while the positive displacement pump intermittently delivers a liquid by using periodically increased and decreased pumping chamber volumes. At the same head and flow rate, the positive displacement pump usually has better efficiency but higher maintenance costs and more complicated pipe systems in comparison with the rotodynamic pump.

Rotodynamic pumps, such as multistage centrifugal pump [14,15], single-stage centrifugal pump [16], roto-jet pump [14], peripheral or regenerative pump [17] have been tested in ORC systems. Similarly, the axial piston pump [18], sliding vane pump [19,20], plunger pump [16], piston pump [21,22], diaphragm pump [14,23–26], and external gear pump [27] have been investigated experimentally in ORC systems. Even though all these pumps are examples of the positive displacement pump,

* Corresponding author.
E-mail address: Zhibin.yu@glasgow.ac.uk (Z. Yu).

https://doi.org/10.1016/j.tsep.2021.101079
Received 4 April 2021; Received in revised form 8 September 2021; Accepted 9 September 2021
Available online 20 September 2021

Nomenclature

a	constant in Eq. (42)
b	solution constant in Eq. (50)
B	dimensionless factor related to vapour volume fraction defined in Eq. (58)
c_{min}	minimum sound speed of mixture, m/s
c_{pl}	specific heat capacity of liquid, J/kg K
c_{pg}, c_{vg}	specific heat capacities of non-condensable gas at constant pressure and constant volume, respectively, J/kg K
C	constant in Eq. (4)
C_{con}	empirical constant for $\dot{m}_{con}$,
C_{vap}	empirical constant for$\dot{m}_{vap}$
$\mathscr{D}$	thermal diffusivity of liquid, m^2/s
D_n	rate that molecules strike the surface of the clusters with n molecules in Eq. (43)
e	internal energy of mixture, J/kg
e_l	internal energy of liquid, J/kg
erf	Gaussian error function
e_v	internal energy of vapour, J/kg
F_{vap}	empirical constant for evaporation in Eq. (39)
F_{con}	empirical constant for condensation in Eq. (39)
h	heat transfer coefficient across the bubble boundary, J/m^2 K
J	Jakob number defined as Eq. (44)
k	turbulent kinetic energy, m^2/s^2
$K_{l\to v}$	rate of vapour generation, Eq. (8)
$K_{v\to l}$	rate of vapour condensation in Eq. (8)
l_c	cut-off distance characteristic
L	latent heat of liquid, J/kg
m	empirical power in Eq. (40)
$\dot{m}$	phase change rate, kg/m^3 s
$\dot{m}_l$	liquid mass transfer rate, kg/m^3
$\dot{m}_v$	vapour mass transfer rate, kg/m^3 s
M	molecular mass of liquid, g/mol
n	number of molecules in Eq. (43)
ν	polytropic index
n_0	number of vapour bubbles in a unit volume, $1/m^3$
n^*	number of vapour bubbles at$p_{min}=0$
N	population of vapour bubbles in critical size, $1/m^3$ s
N_l	population density of impurity particles or seeding nuclei in liquid, $1/m^3$
p	local pressure of mixture, Pa
p_1	pressure at pump inlet, kPa
p_g	partial pressure of non-condensable gas in a bubble, Pa
p_{g0}	initial partial pressure of non-condensable gas in a bubble, Pa
p_l	liquid pressure, Pa
p_{min}	minimum pressure in the throat of a nozzle, Pa
p_t	pressure due to velocity turbulent fluctuation, Pa
p_v	local vapour pressure, Pa
p_{vortex}	pressure profile in a cavitating Rankine vortex, Pa
r	radial coordinate of the spherical or cylindrical coordinate system, m
R	vapour bubble radius, m
R_{core}	central core radius of Rankine vortex, m
R_0	initial radius of vapour bubble, m
R_{0max}	maximum initial nuclei size, m
R_{0min}	minimum initial nuclei size, m
R_g	bubble radius of non-condensable gas in liquid, m
R_{g0}	bubble initial radius of non-condensable gas in liquid, m
R_{gas}	universal gas constant, J/K mol
R^+	dimensionless vapour bubble radius defined in Eq. (51)
s_l	specific entropy of liquid, J/kg K
s_{lv}	specific entropy of liquid and vapour mixture, J/kg K
S_{ij}	time-averaged velocity deformation rate tensor in Eq.(73), 1/s, $i,j=1,2,3$
S_{max}	maximum shear rate in two-dimensional flow field in Eq. (75), 1/s
t	time, s
t_∞	mean time scale of liquid, s
t^+	dimensionless time defined in Eq. (51)
T_l	temperature of liquid, ℃, K
T_∞	temperature of liquid in far-field, ℃, K
$\varkappa$	net average velocity of vapor molecules in Eq. (11), m/s
u_i, u_j	time-averaged velocity components in the Cartesian coordinate system in i and j coordinate directions, m/s, $i,j=1,2,3$
u_∞	free stream velocity of liquid, m/s
v_l	specific volume of liquid, m^3/kg
v_v	specific volume of vapour, m^3/kg
$\dot{v}_{con}$	condensation mass transfer rate, 1/s
$\dot{v}_{vap}$	evaporation mass transfer rate, 1/s
W	minimum work, J
W_{min}	minimum work related to the cut-off distance characteristic l_c at zero surface tension in Eq. (43), J
x_i	Cartesian coordinates in a flow field, m, i=1,2,3
y	vapour mass fraction
z	number of nearest neighbouring molecules surrounding a single molecule in Eq. (43)
Z_f	Zeldovich non-equilibrium factor in Eq. (43)

Greek

α_0	initial nuclei volume fraction
α_l	liquid volume fraction
α_{nc}	nucleation site volume fraction in liquid
α_v	vapour volume fraction
γ	surface tension of liquid, N/m
Γ	Rankine vortex circulation, m^2/s
δ	geometrical parameter depending on vapour bubble shape in Eq. (42), °
Δp	pressure width in Eq. (6), Δp=150 Pa for water
Δp_v	pressure depression, $\Delta p_v=p_v(T_\infty)-p_v$, Pa
ΔT	temperature depression, $\Delta T=T_\infty-T_v$, ℃, K
ζ	auxiliary variable in Eq. (24)
η	constant in Eq. (6)
θ	half angle of the bubble surface measured at the centre of the surface curvature in Eq. (42), °
ι	auxiliary variable in Eq. (24)
κ	Boltzmann constant
λ	thermal conductivity of liquid, W/m K
Λ	factor considering deviation of velocity distribution of vapor molecules in the vicinity of the interface from the Maxwellian probability distribution in Eq. (11)
μ	dynamic viscosity of liquid, Pa s
μ_t	turbulent eddy viscosity, Pa s
ν	kinematic viscosity of liquid, m^2/s
ξ	auxiliary variable in Eq. (24)
ρ	density of liquid, kg/m^3
ρ_g	non-condensable gas density in liquid, kg/m^3
ρ_l	liquid density, kg/m^3
ρ_v	vapour liquid, kg/m^3
σ_{11}	first principal stress in flow field, Pa
υ	auxiliary variable in Eq. (51)
φ	crank angle,°
$\chi(R_0)$	function of gas nuclei distribution in liquid
ψ	auxiliary variable in Eq. (51)
ω	rate of dissipation per unit turbulent kinetic energy, 1/s

Subscripts

i	coordinate index of the Cartesian coordinate system, i=1,2,3
j	coordinate index of the Cartesian coordinate system, j=1,2,3

Abbreviations

1D	one-dimensional
2D	two-dimensional
3D	three-dimensional
CATUM	Cavitation Technical University Munich
CFD	computational fluid dynamics
DBM	discrete bubble model
EOS	equation-of-state
HFO	hydrofluoroolefin
LES	large eddy simulation
MOGA-II	multi objective genetic optimization algorithm
NPSH	net positive suction head
NPSHr	net positive suction head required
ORC	organic Rankine cycle
PDF	probability density functions
RBFNN	radial basis function neural network
SAO	sequential approximate optimization
SST	shear stress transport
UDF	user-defined function
VOF	volume of fluid
ZGB	Zwart, Gerber and Belamri

the sliding vane pump and external gear pump belong to the sub-group of rotary pumps and the rest are reciprocating pumps, as summarised in Fig. 1b. In these experiments, the organic/inorganic fluids, namely R11, R113, R123, R134a, R404, R245fa, HEF-7100, and mixture NH_3/H_2O were used as working medium.

In comparison with rotodynamic pumps, these studies confirmed that positive displacement pumps are more favourable for ORC systems in terms of exergy destruction rate, heat absorption rate, and thermal and exergy efficiencies. However, positive displacement pumps may be subject to a higher net positive suction head required (NPSHr) (0.24 bar) [23,24] or severer subcooling (4.4–20) ℃ [21–24]. NPSHr represents the suction performance of a feed pump when cavitation occurs in it at a low suction pressure. The lower the NPSHr, the better the suction performance, and the safer the pump operation. Essentially, cavitation is a boiling phenomenon in a liquid due to a reduced static pressure at nearly constant liquid temperature. Cavitation results in a cavity in the liquid, the cavity will shrink and collapse when the pressure rises to generate pressure shockwave and performance oscillation or even material damage. Cavitation often appears on the blade suction side near the blade leading edge in centrifugal and roto-jet pumps, in the suction port/

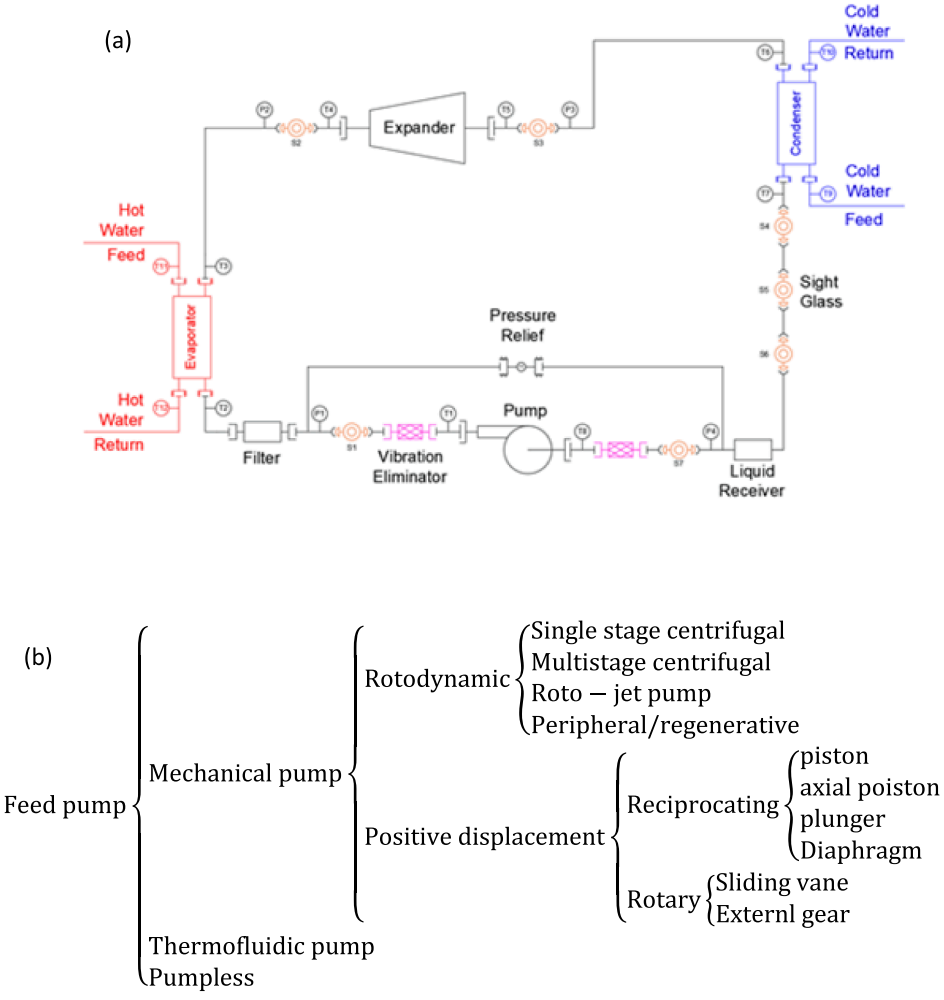

Fig. 1. The feed pumps used in existing ORC systems, (a) ORC test loop, (b) classification of feed pumps, (a) is after [29].

chamber in regenerative, axial piston, sliding vane, and gear pumps, in the suction valve in plunger, piston and diaphragm pumps, respectively. The locations of cavitating cavity in a specific diaphragm pump predicted with computational fluid dynamics (CFD) simulation are illustrated in Fig. 2, where the cavities appear in the gap between the seat and the valve, and on the valve surface.

Since the phase change of liquid to vapour needs latent heat, a temperature difference or temperature depression (liquid temperature minus vapour temperature) exists across the boundary between the liquid outside the cavity and the vapour inside the cavity. The magnitude of temperature depression depends on thermophysical property of liquid. The temperature depression in cavitation is considered as thermodynamic effect. To characterise the thermodynamic effect in cavitation the following dimensional thermodynamic parameter Σ is defined as [28]

$$\Sigma = \frac{L^2 v_l^2}{T_l c_{pl} v_v^2 \sqrt{\mathscr{D}}} \tag{1}$$

where L is the latent heat of a liquid at liquid temperature T_l, v_l is the specific volume of the liquid, c_{pl} is the specific heat capacity of the liquid, $\mathscr{D}$ is the thermal diffusivity of the liquid, $\mathscr{D} = \lambda/\rho_l c_{pl}$, v_v is the specific volume of the vapour, λ is the thermal conductivity of the liquid, ρ_l is the density of the liquid. In Fig. 3, the thermodynamic parameter Σ is plotted as a function of liquid temperature $T_l$for the banned organic fluid R113, the organic fluids being phased out such as R123 and R134a, and the promising hydrofluoroolefin (HFO) organic fluid R1234yf. The thermodynamic parameter Σ of water and nitrogen is also included in the figure for reference. The thermodynamic parameter Σ is a proportional constant between the vapour bubble radius growth or collapse rate with time and the temperature depression. The larger the thermodynamic parameter, the smaller the radius growth or collapse rate at a constant temperature pression, and the more significant thermodynamic effect in cavitation, or vice versa [28]. The thermodynamic

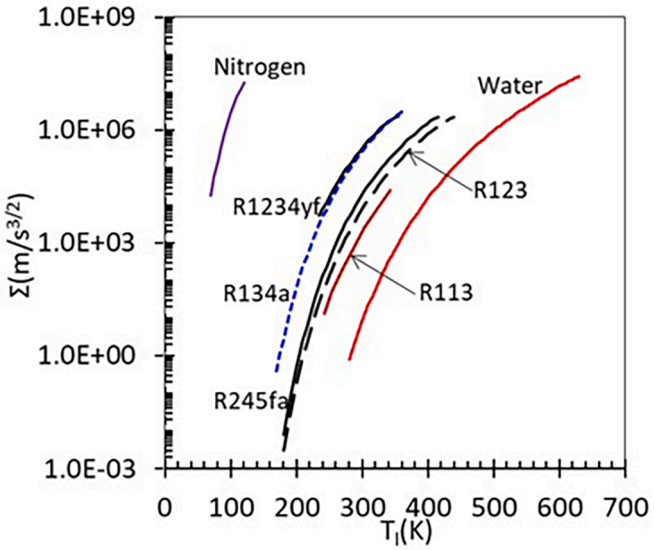

Fig. 3. The thermodynamic parameter Σ curve versus liquid temperature T_l for water, R113, R123, R134a, R245fa, R1234yf and nitrogen.

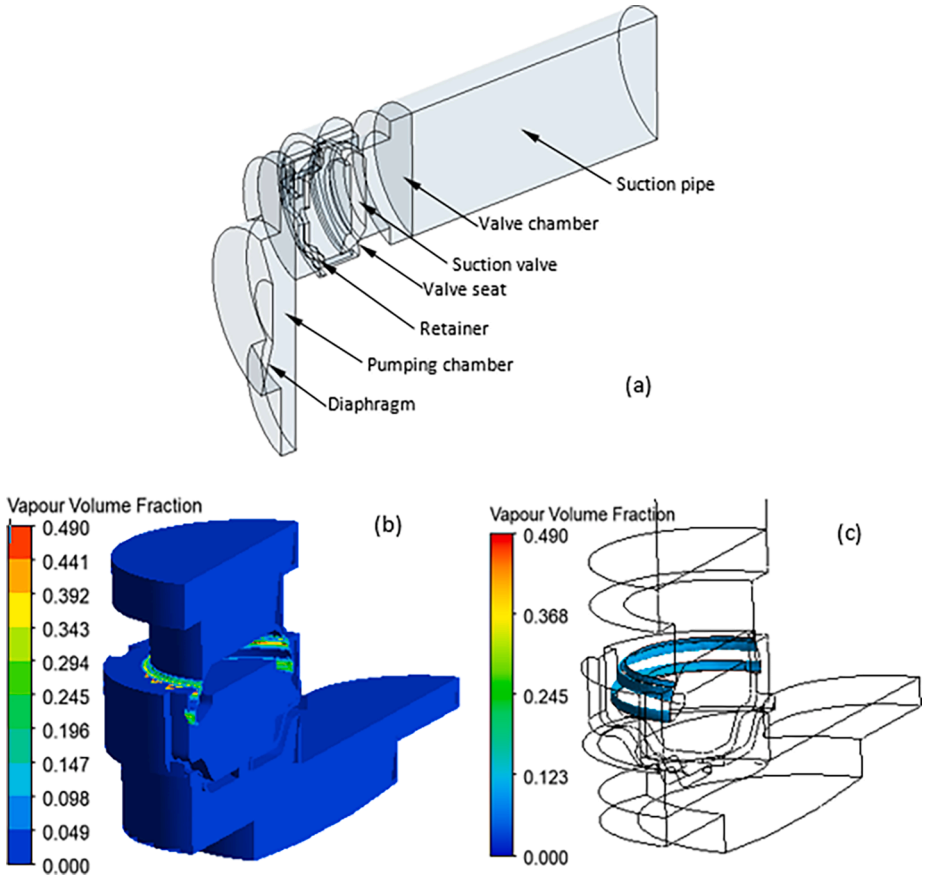

Fig. 2. The geometrical model of the liquid end of a diaphragm pump for CFD simulation (a), the contours of vapour volume fraction (b), and the *iso*-surface of vapour volume fraction of 0.1 (c) at the inlet pressurep_1 = 85.2 kPa and the crank angleφ = 106.2° as well as rotational speed of 480 rpm, the liquid end is symmetrical, thus a half model is adopted in the simulation, the spring for the valve is considered in the valve rigid body equation, the picture are .
adapted from [36]

parameter of the organic fluids presented in Fig. 3 is in between water (weakest thermodynamic effect) and nitrogen (strongest thermodynamic effect). This fact suggests that the thermodynamic effect exhibited in cavitation of organic fluids should be taken into account in determining the cavitation performance of a pump when it is applied in an ORC system to deliver an organic fluid [29]. Determining NPSHr or subcooling of the pump during feeding an organic fluid is one important issue in the design and operation of ORC systems as it will significantly influence the stability of the system and impair the evaporator performance.

CFD has been increasingly employed to study cavitation with thermodynamic effect when thermo-sensitive liquids flow around hydrofoils, in nozzles and through centrifugal pumps. CFD simulations of cavitation in reciprocating pumps have been conducted in the absence of the thermodynamic effect using cold water [30–35]. However, there has been little CFD investigation into cavitation performance and flow details in reciprocating pumps when the pumps delivering organic fluids with thermodynamic effect in ORC systems so far because this effect of organic fluids was not noticed considerably by researchers [36].

With this in mind, we will investigate unsteady cavitation flows of an organic fluid with thermodynamic effect in a reciprocating pump for ORC systems based on CFD simulations along with experimental observations. The work includes cavitation model development with thermodynamic effect for organic fluids, CFD implementation, validation and CFD simulations under various inlet pressure and rotative speed conditions. To help establish reliable cavitation models, a comprehensive survey of cavitation models for CFD is imperative.

There have been excellent reviews of cavitation models in the literature [37–41]. For example, the modelling and computational strategies for simulating cryogenic cavitation relevant to liquid rocket propulsion applications were reviewed in [37]. The homogeneous cavitation models and turbulence closure for unsteady cavitating flows were discussed in [38]. The homogeneous cavitation models published after 2010 were presented in [39]. The unsteady cavitating flow modelling and brief survey on cavitation models were devoted to hydraulic machines and hydrofoils in [40] and [41], respectively.

The research that had been covered by the review articles above will be omitted herein. This article will be focused on the new developments in cavitation models after 2016 and the previous cavitation models associated with thermodynamic effect. The review will form a framework of cavitation model selection, model generation and validation for CFD simulations of the cavitating flow of an organic fluid in the feed pumps of ORC systems.

2. Classification of cavitation models

Numerical simulation of cavitating flows has been a challenging subject since the 1960′s, much is still unknown about phenomena, such as compressible and incompressible flows, relative slip motion between the cavitating bubbles/cavity and the liquid, and phase change, coexist in a flow domain [42]. Cavitation models are crucial in the numerical simulation of cavitating flows. Based on the feature of cavitation models in mathematics, the cavitation models can be classified into deterministic models and stochastic models at first. The deterministic models are divided into three categories: (1) interface tracking models, (2) homogeneous two-phase mixture models, and (3) multiscale models, according to their feature in physics. In the interface tracking models, there is no sub-class but are five models. In the homogeneous two-phase mixture models, there are five sub-classes such as equation-of-state (EOS), arbitrary mass transfer rate, evaporation and condensation, Rayleigh-Plesset equation-based, and nucleation model groups. In the EOS model class, further eight sub-classes, namely liquid–vapour thermodynamic variable table, first-order differential equation of density, barotropic law curve without vapour volume fraction transport equation, sinusoidal barotropic law without vapour volume fraction transport equation, sinusoidal barotropic law with vapour volume fraction transport equation, stiffened gas law without vapour volume fraction transport equation, stiffened gas law with vapour volume fraction transport equation, and Gibbs free energy for phase mixture. There are not sub-classes in the arbitrary mass transfer rate, evaporation and condensation model groups. In the Rayleigh-Plesset equation-based model group, Schnerr-Sauer model, full cavitation model, ZGB model, unified model, cavitation models with liquid viscosity, Rankine vortex cavitation model, cavitation models with bubble–bubble interaction, cavitation models with bubble breakup in cavity cloud, and cavitation models with first principal stress can be divided further. In the nucleation cavitation models, five sub-classes i.e., nuclei number density distribution of power function, nuclei number density distribution of exponential function, vapour nucleation theory with Rayleigh-Plesset equation, vapour nucleation theory with empirical function of nuclei number density distribution and vapour nucleation theory with existing simplified cavitation models in CFD package appear. In the multiscale models, one-way and two-way coupling model groups exist. In the one-way coupling cavitation model group, four sub-classes such as model for cavitation inception, fully developed cavitation model in still liquid, fully developed cavitation model in flowing liquid and Euler-Lagrange sheet and bubble cavitation model are present. In the two-way coupling cavitation models, there is one class only, e.g., the Euler-Lagrange fully developed cavitation model. Since the stochastic model is newly developed, it is not classified further, and has one model only.

This proposed classification of cavitation models is elucidated in Fig. 4. A detailed classification of cavitation models is illustrated in Table 1. The classification method in this article can deal with most existing cavitation models in the literature. In the following sections, the cavitation models presented in Table 1 will be reviewed and discussed.

2.1. Interface tracking models

In interface tracking models, the cavity and liquid interface is tracked based onp_v = constant condition in two-dimensional (2D) or axis-symmetrical steady inviscid flows [43–46], where p_v is the vapour pressure of a liquid. The model was expanded to 2D viscous flows by solving 2D incompressible Navier-Stokes equations [47] and energy equation with artificial compressibility algorithm and introducing thermodynamic effect in cavitation [48,49]. Particularly, thermodynamic effect is involved by using the heat balance equation across the interface and implemented in the energy equation as a boundary condition-temperature gradient in the interface normal direction. In the cavitation model, p_v, and ρ_v/ρ_l are treated as temperature-dependent parameters [49], where ρ_v and ρ_l are vapour and liquid densities, respectively. The interface tracking model has been challenged in dealing with three-dimensional (3D) cavitation problems.

2.2. Homogeneous two-phase mixture models

In homogeneous two-phase mixture models, the fluid is either a liquid or a variable density homogeneous two-phase mixture of the liquid and its vapour. In a homogeneous mixture, the liquid and vapour are in mechanical and thermal equilibrium and share the same velocity and pressure. In the homogeneous two-phase mixture models, the continuity equation, momentum equations, transport equation for the number of bubbles or vapour/liquid volume fraction and energy (temperature) equation (for cavitation with thermodynamic effect) need to be solved simultaneously. The EOS model, arbitrary mass transfer rate model, Rayleigh-Plesset equation-based mass transfer rate model and nucleation model are four common cavitation models in this category.

In EOS models, a vapour void fraction transport equation can be included. In doing so, the cavitation process is reflected by the mass transfer source terms in the equation, or the process is represented by the vapour void fraction which determined with the EOS models themselves. However, a vapour volume fraction transport equation is not needed in most EOS models.

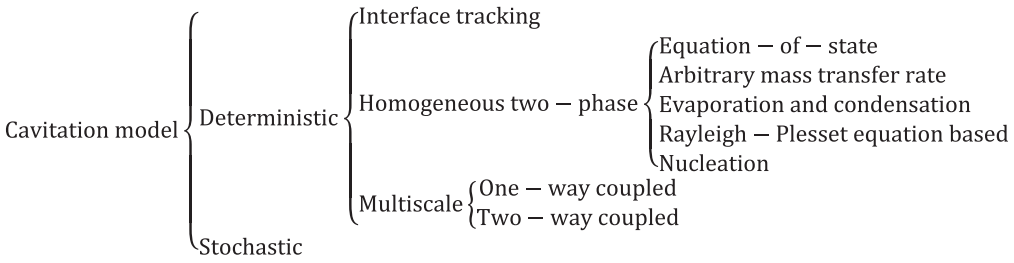

Fig. 4. The proposed classification of cavitation models.

In homogeneous two-phase mixture models, non-condensable gas in a liquid can be included. In that case, the non-condensable gas yields the ideal gas law (isothermal process) or polytropic law and shares the same velocity and pressure with the rest phase but doesn't have phase change. The methods for accounting for non-condensable gas in cavitation models are interpreted in the discussion section.

2.2.1. EOS models

In EOS models, the liquid or the mixture of the liquid and its vapour is steady, inviscid and barotropic ($\rho = \rho(p)$, where ρ is the density of the mixture), and thus dismisses the necessity for an energy equation [50]. A phase change model was developed for the cavitation with thermodynamic effect where the vapour mass fraction y depends on the liquid entropy gradient ds_l/dp_v, entropy of mixture s_{lv} and the difference between the vapour pressure p_v and local pressure p. This is defined in Eq. (2) [50]:

$$y = \left(\frac{ds_l}{dp_v}\right)\left(\frac{p_v - p}{s_{lv}}\right) \tag{2}$$

where y is related to the mixture density ρ as $p < p_v$ by Eq.(3)

$$\rho = \frac{1}{\frac{1}{\rho_l} + y\left(\frac{1}{\rho_v} - \frac{1}{\rho_l}\right)} = \frac{1}{\frac{1}{\rho_l} + \left(\frac{ds_l}{dp_v}\right)\left(\frac{p_v - p}{s_{lv}}\right)\left(\frac{1}{\rho_v} - \frac{1}{\rho_l}\right)} \tag{3}$$

where $\rho = \rho_l$ as $p \geq p_v$. This is the first phase change model for cavitation with thermodynamic effect. Based on a known table of saturated liquid–vapour thermophysical properties, the density of the liquid–vapour mixture can be determined at a temperature and pressure with Eq.(3). This EOS model is called liquid–vapour thermodynamic variable table-based model or density-based model. Similar models can be found in [51,52]. With the density-based model, the software, named CATUM (Cavitation Technical University Munich) for solving 3D, unsteady, compressible, various Mach numbers, cavitating flows with time-step as short as a nanosecond was developed to capture the shockwave generated by vapour bubble collapse in [52]. In this model, the vapour volume fraction transport equation is not needed.

Another EOS model for isothermal cavitation was established by using a first-order differential equation of liquid–vapour mixture for axisymmetric unsteady viscous flows [53] and for 2D unsteady flows around a hydrofoil [54]. In the model, the change rate of the two-phase mixture density $d\rho/dt$ is assumed to be proportional to the difference between the local pressure p and the vapour pressure p_v as:

$$d\rho/dt = C(p - p_v) \tag{4}$$

where C is a constant depending on Reynolds number [54]. The model does not require the vapour volume fraction transport equation.

The barotropic law curve is an important EOS model for cavitation. In the model, the density of water-vapour mixture was plotted as a function $\rho = f(p)$ with four parameters ρ_v, ρ_l, p_v and minimum sound speed c_{min} [55–57]. The curve can be fitted by using a sine function as [58]:

$$\rho = \frac{\rho_l + \rho_v}{2} + \frac{\rho_l - \rho_v}{2}\sin\left(\frac{p - p_v}{c_{min}^2 \frac{\rho_l - \rho_v}{2}}\right), \text{ and } \alpha_v = \frac{\rho_l - \rho}{\rho_l - \rho_v} \tag{5}$$

where c_{min} is adopted to control the slope of the curve, and the value of the sine function is in the range of $[-1, 1]$. If ρ is known, the vapour volume fraction or vapour void fraction α_v is calculated more easily. This model does not need the vapour void fraction transport equation and was implemented in the CFD software-FINE TURBO [56–58].

A sinusoidal barotropic law was proposed in [59,60]. The mixture pressure is expressed by vapour void fraction in the model based on Eq. (5) when the pressure is in the range of $[p_v - \Delta p, p_v + \Delta p]$:

$$p = p_v + c_{min}^2 \frac{\rho_l - \rho_v}{2} \sin^{-1}[\eta(1 - 2\alpha_v)] \tag{6}$$

where $\sin^{-1}()$ represents the inverse function of sin(), Δp is the pressure width of the law, Δp=150 Pa for water [60], the model constants c_{min} and η are determined with the continuity conditions of the pressure and the speed of sound between the liquid and the mixture at $p = p_v + \Delta p$ [59]. From Eq. (6), the speed of sound of the mixture can be calculated by taking $dp/d\rho$. This model does not request the vapour void fraction transport equation essentially.

The sinusoidal barotropic law Eq.(6) was used together with a vapour void fraction transport equation which includes the mass transfer source terms for vaporization and condensation in cavitation [61–65]. Eq.(6) is nothing more than supplying an analytical relationship between pressure and density for a liquid–vapour mixture.

Water can be considered compressible in cavitation, especially in vapour bubble collapse stage. Thus, the relationship of pressure with density and internal energy can be described by using stiffened (convex) EOS (its second derivative is nonnegative in its entire domain), i.e., stiffened gas law, which is usually for gas. Since both water and its vapour are compressible, the numerical procedure is simplified, and the numerical solution converges easily. A stiffened gas law of the EOS model was deduced in [59,66]. Firstly, the stiffened gas law was built for each phase (the liquid phase is subject to low Mach number preconditioning). Then the thermodynamic variables of the mixture were deduced from the thermal and mechanical equilibrium as an analytical function of vapour void fraction. Particularly, the vapour void fraction is determined simply by the internal energy of each phase at saturation [59]:

$$\alpha_v = \frac{\rho e - \rho_l e_l}{\rho_v e_v - \rho_l e_l} \tag{7}$$

where e, e_l and e_v are the internal energy of the mixture, liquid and vapour, respectively. The vapour void fraction transport equation is not required.

The stiffened gas law could also be employed along with the vapour void fraction transport equation like the sinusoidal barotropic law Eq. (6). In this case, the mass transfer source terms for vaporization and condensation in cavitation are involved [61,62,67].

These EOS-based models take the most dominant advantage that the thermodynamic effect in cavitation can enter the model as long as the

Table 1
Classification, contributor, and feature of existing cavitation models for CFD simulations.

First-class	Second-class	Third-class	Fourth-class	Contributor (year)	Number of models	Feature	Source
Deterministic	Interface tracking	No	No	Brennen (1969); Lemonnier & Rowe (1988); Pellone & Rowe (1988); Deshpande, Feng & Merkle (1994); Liu, Li & Feng (2006)	4	1. 2D fluid flows; 2. Cavity and liquid interface is tracked with p_v = constant.	[43–47]
	Homogeneous two-phase mixture	Equation-of-state models	Liquid-vapour thermodynamic variable table	Cooper (1967); Ventikos & Tzabiras (2000); Schnerr, et al (2008)	3	1. Thermophysical variables of liquid and vapour in saturation are known in a table in terms of pressure and temperature. 2. Vapour volume fraction is interpolated or calculated with known thermophysical variables of mixture from governing equations and those of liquid and vapour in the table.	[50–52]
			First-order differential equation of density	Chen & Heister (1995); Okita & Kajishima (2002)	2	1. It is assumed $d\rho/dt = C(p - p_v)$. 2. Density or vapour volume fraction is calculated from that equation.	[53,54]
			Barotropic law curve without vapour volume fraction transport equation	Delannoy & Kueny (1990); Coutier-Delgosha, Reboud & Delannoy (2003); Reboud, Coutier-Delgosha, Pouffary, et al (2003)	3	1. Density curves of water-vapour mixture are plotted against pressure at minimum sound speed c_{min} = 0.5, 2 m/s. 2. Vapour volume fraction is $\alpha_v = (\rho - \rho_v)/(\rho_l - \rho_v)$.	[55–57]
			Sinusoidal barotropic law without vapour volume fraction transport equation	Goncalves & Patella (2009); Decaix & Goncalves (2013)	3	1. $p = p_v + \left(\frac{\rho_l - \rho_v}{2}\right) c_{min}^2 sin^{-1}[A(1-2\alpha_v)]$. 2. Vapour volume fraction is $\alpha_v = (\rho_l - \rho)/(\rho_l - \rho_v)$.	[59,60]
			Sinusoidal barotropic law with vapour volume fraction transport equation	Goncalves & Patella (2011); Goncalves (2013); Goncalves (2014); Goncalves & Charriere (2014); Goncalves & Zeidan (2017)	5	1. $p = p_v + \left(\frac{\rho_l - \rho_v}{2}\right) c_{min}^2 sin^{-1}(1-2\alpha_v)$. 2. Vapour volume fraction is determined by solving its transport equation.	[61–65]
			Stiffened gas law without vapour volume fraction transport equation	Goncalves & Patella (2009, 2010)	2	1. Thermophysical variables of mixture are calculated by stiffened gas law of each phase. 2. Vapour volume fraction is calculated with internal energy of each phase in saturation.	[59,66]
			Stiffened gas law with vapour volume fraction transport equation	Goncalves & Patella (2011); Goncalves (2013); Goncalves (2014); Charriere, Decaix & Goncalves (2015)	4	1. Thermophysical variables of mixture are calculated by stiffened gas law of each phase. 2. Vapour volume fraction is estimated by solving its transport equation.	[61–63,67]
			Gibbs free energy for phase mixture	Vortmann, Schnerr & Seeleck (2003)	1	1. Based on phase change model of shape memory alloys. 2. Cavitation occurrence depends on Gibbs free energy of the phase mixture.	[68]
		Arbitrary mass transfer rate models	No	Merkle, Feng & Buelow (1998); Kunz, Boger, Stinebring, et al (2002); Senocak & Shyy (2004)	4	1. Cavitation mass transfer rate is proportional to $p - p_v$.	[69–71]
		Vapor-liquid interface evaporation and condensation model	No	Saito, Takami, Nakamori, et al (2007); Liu, Li, Zhang, et al (2008); Ochiai, Iga, Nohmi, et al (2010); Gnanaskandan & Mahesh (2015); Le, Okajima & Iga	6	1. Evaporation and condensation occur on liquid–vapour interface. 2. Both depend on pressure and temperature of two phases, yield Schrage's formula.	[81–86]

(*continued on next page*)

Table 1 (*continued*)

First-class	Second-class	Third-class	Fourth-class	Contributor (year)	Number of models	Feature	Source
				(2019); Yang & Habchi (2020)			
		Rayleigh-Plesset equation-based mass transfer rate model	Schnerr-Sauer model	Schnerr & Sauer (2001); Yuan, Sauer & Schnerr (2001); Kanfoud, Lamloumi & Zgolli (2010)	3	1. Relation of α_v to n_0 and R is correct. 2. dR/dt is determined with Rayleigh-Plesset equation.	[89,91,98]
			Full cavitation model	Singhal, Athavale, Li, et al (2002); De Giorgi, Bello & Ficarella (2010); Tsuda, Tani & Yamanishi (2012); Zhang, Wu, Xiang, et al (2013)	4	1. Relation of α_v to n_0 and R is approximate. 2. dR/dt is determined with Rayleigh-Plesset equation. 3. R is determined by Weber number.	[103–106]
			ZGB model	Zwart, Gerber & Belamri (2004)	1	1. Relation of α_v to n_0 and R is approximate. 2. dR/dt is determined with Rayleigh-Plesset equation. 3. R is initial nuclei size R_0.	[109]
			Unified model	Kinzel, Lindau & Kunz (2017)	1	1. Mass transfer rate equation is with more exponents and coefficients. 2. Different exponents and coefficients correspond to different Rayleigh-Plesset based cavitation models.	[121]
			Cavitation models with liquid viscosity	Yu, Luo, Ji, et al (2014); Pang, Li, Yang, et al (2018)	2	1. Based on ZGB model. 2. dR/dt is determined by Rayleigh-Plesset equation with liquid viscosity.	[201,202]
			Rankine vortex cavitation model	Zhao, Wang & Huang (2016)	1	1. Cavity is the core of Rankine vortex. 2. Core size yields Rayleigh-Plesset equation.	[204]
			Cavitation models with bubble–bubble interaction	Ye & Li (2016); Ye, Zhu, Lai, et al (2017)	2	1. Based on ZGB model. 2. dR/dt is determined with Rayleigh-Plesset equation with bubble–bubble interaction.	[212,213]
			Cavitation models with bubble breakup in cavity cloud	Du, Wang, Liao, et al (2016); Du, Wang, Huang, et al (2017)	2	1. Based on full cavitation model. 2. Mass transfer rate in condensation is modified by considering bubble breakup in cavitation cloud.	[215,216]
			Cavitation models with first principal stress	Asnaghi, Feymark & Bensow (2017); Hong, Gao, Liu, et al (2018)	2	1. Based on Schnerr-Sauer model. 2. First principal stress is used as cavitation criterion. 3. The criterion is for 2D turbulent flows only.	[219,220]
		Nucleation cavitation models	Nuclei number density distribution of power function	Kumar and Brennen (1993); Wang (1999)	2	Nuclei size profile was fitted by initial nuclei volume fraction, minimum and maximum initil nuclei sizes and power function of R_0.	[129,130]
			Nuclei number density distribution of exponential function	Liu and Brennen (1998)	1	Nuclei size profile was fitted by three constants and exponential function of R_0.	[127]
			Vapour nucleation theory with Rayleigh-Plesset equation	Takemura & Matsumoto (1994); Ito, Wakamatsu & Nagasaki (2003); Ito (2008), Ito, Zheng & Nagasaki (2019); Delale, Okita & Matsumoto (2005)	5	Classical nucleation theory is involved in vapour bubble mass conservation equation as a source term.	[140–144]
			Vapour nucleation theory with empirical function of nuclei number density distribution	Li, Liu, Wei, et al (2018)	1	1. Empirical function of nuclei number density distribution and vapour nucleation theory are combined. 2. Non-condensable gas concentration and partial pressure are considered. 3. dR/dt is determined with Rayleigh-Plesset equation.	[145]
					2		[147,148]

(*continued on next page*)

Table 1 (*continued*)

First-class	Second-class	Third-class	Fourth-class	Contributor (year)	Number of models	Feature	Source
			Vapour nucleation theory with existing simplified cavitation models in CFD package	De Giorgi, Ficarella & Fontanarosa (2019, 2020)		Vapour nucleation theory is coupled with Schnerr-Sauer cavitation model with vapour volume fraction.	
	Multiscale	One-way coupling	Model for cavitation inception	Kodama, Take, Tamiya, et al (1981); Meyer, Billet & Holl (1992); Hsiao, Chahine & Liu (2003); Oweis, van der Hout, Iyer, et al (2005); Hsiao & Pauley (1999); Farrell (2003); Hsiao & Chahine (2004,2005)	7	1. Flow field is known. 2. Nuclei trajectory is tracked by using Corrsin and Lumley equation. 3. Nuclei size is determined with Rayleigh-Plesset equation.	[149–152,154–157]
			Fully developed cavitation model in still liquid	Okuda & Ikohagi (1996); Matsumoto & Yoshizawa (2005); Ochiai & Ishimoto (2017,2020); Johnsen & Colonius (2008,2009)	4	1. Vapour bubble array or single bubble is in still liquid. 2. Mixture of liquid-bubble is compressible. 3. Bubble collapse is modelled.	[159–164]
			Fully developed cavitation model in flowing liquid	Nohmi, Ikohagi & Iga (2008); Ochiai, Iga, Nohmi et al (2013); Khojasteh-Manesh & Mahdi (2019)	3	1. Flow of mixture of vapour and liquid is calculated. 2. Vapour bubble trajectory is tracked. 3. Bubble size is determined with Rayleigh-Plesset equation. 4. Pressure field near solid wall is reanalysed and damage rate to the wall is predicted.	[165,167,169]
			Euler-Lagrange sheet and bubble cavitation model	Li, Wang, Li, et al (2021)	1	1. Flow of mixture of vapour and liquid is simulated. 2. Vapour bubble trajectory is calculated. 3. Bubble size is decided with simplified Rayleigh-Plesset equation. 4. Total vapour volume fraction is equal to sum of those obtained in 1 & 2 simulations.	[179]
		Two-way coupling	Euler-Lagrange fully developed cavitation model	Kubota, Kato & Yamaguchi (1992); Ishimoto & Kamijo (2003); Giannadakis, Gavaises & Arcoumanis (2008); Abdel-Maksoud, Hanel & Lantermann (2010); Ma, Hsiao & Chahine (2015,2017); Hsiao, Ma & Chahine (2017); Hammerl & Wall (2015); Peters & el Moctar (2020)	8	1. Flow of mixture of vapour and liquid is calculated. 2. Vapour bubble trajectory is tracked. 3. Bubble size is determined with Rayleigh-Plesset equation. 4. Three processes are coupled.	[171–178,180]
Stochastic	Stochastic field	No	No	Dumond, Magagnato &Class (2013)	1	1. Rayleigh-Plesset equation and a probability density function of bubble size are used. 2. Stochastic field method is employed.	[207]

thermophysical property constants are expressed as a function of temperature or the vapour pressure is updated with a linear relationship between pressure depression Δp_v $(=p_v(T_\infty)-p_v)$ and temperature depression ΔT $(=T_\infty - T_v)$ $\Delta p_v = (dp/dT)\Delta T$ [61,63,65,66]. Here, T_∞ is far-field liquid temperature, where dp/dT is calculated from a barotropic law above, T_v is the vapour temperature. One disadvantage of these models is that there are too few adjustable parameters to fit experimental data. As a result, the models may lose the applicability to a variety of cavitating flows.

Recently, a Gibbs free energy function-based isothermal cavitation model was provided in terms of the original concept of deformation for shape memory alloys. The phase change rate equation is expressed as

$$dy/dt = (1-y)K_{l\to v} - yK_{v\to l} \tag{8}$$

where y is vapour mass fraction, $K_{l\to v}$ is the rate of vapour generation and $K_{v\to l}$ is the rate of vapour condensation. The rates depend on the

Gibbs free energy function [68] for axisymmetric inviscid unsteady flows. The vapour void fraction transport equation needs to be solved in the model.

2.2.2. Arbitrary mass transfer rate models

An arbitrary mass transfer rate model was proposed for the liquid volume fraction transport equation in terms of $p-p_v$ in [69] for isothermal cavitation as done in [51]. In this model, the transport equation is expressed as

$$\frac{d\alpha_l}{dt}=\dot{v}_{vap}+\dot{v}_{con},\dot{v}_{vap}=\frac{C_{vap}\max(p-p_v,0)(1-\alpha_l)}{t_\infty\left(0.5\rho_l u_\infty^2\right)},\dot{v}_{con}=\frac{C_{con}\rho_l\min(p-p_v,0)\alpha_l}{\rho_v t_\infty\left(0.5\rho_l u_\infty^2\right)} \tag{9}$$

where α_l is liquid volume fraction,$\dot{v}_{vap}$ is evaporation volume transfer rate, $\dot{v}_{con}$ is condensation volume transfer rate, C_{con} and C_{vap} are the empirical constants for $\dot{v}_{con}$ and $\dot{v}_{vap}$, t_∞ is mean time scale of liquid, u_∞ is free stream velocity of liquid. Its updated version can be found in [70] with an updated $\dot{v}_{vap}$ expression and non-condensable gas volume fraction used in [71].

Eq.(9) was applied to predict the cavitating flows with thermodynamic effect around a hydrofoil [72–77] and an inducer [78], by solving the energy equation and allowing thermophysical property constants to depend on liquid temperature.

2.2.3. Vapor-liquid interface-based evaporation and condensation models

When a liquid and its own vapour contact with each other, the liquid evaporates, or the vapour condenses depending on the pressure and temperature of the two phases. Usually, the process of vaporization is simpler than condensation, the well-known net mass transfer rate across the liquid–vapour interface is calculated by using Schrage's formula for non-equilibrium condensation [79]

$$\dot{m}=\sqrt{\frac{M}{2\pi R_{gas}}}\left(\frac{p_l}{\sqrt{T_l}}-\Lambda\frac{p_v}{\sqrt{T_v}}\right) \tag{10}$$

where $\dot{m}$ is cavitation mass transfer rate, M is the molecular mass of a liquid, R_{gas} is the universal gas constant,p_l and T_l are the liquid pressure and temperature,p_v and T_v are the vapour pressure and temperature, respectively, Λ is a factor accounting for the deviation of the velocity distribution of the vapor molecules in the vicinity of the interface from the Maxwellian probability distribution, and reads as

$$\Lambda=\exp\left(-\frac{M\nu^2}{2\pi T_v}\right)-\sqrt{\frac{\pi M}{2R_{gas}T_v}}\nu\,\mathrm{erf}\left(\sqrt{\frac{\pi M}{2R_{gas}T_v}}\nu\right) \tag{11}$$

where ν is a net average velocity of the vapor molecules, erf is defined as the Gaussian error function. Eq.(11) is initially used as a cavitation model of water when a single vapour bubble collapses in water in [80].

For water and its vapour flows, a compressible viscous two-phase mixture flow model was proposed in [81,82]. The speed of sound is an analytical expression of vapour void fraction. The phase change rate per unit area at the interface between the two phases is based on Eq.(10) with the simplification of $\Lambda=1$ and $T_v=T_l$. As a result, the phase change rate for the vapour mass fraction equation is written as

$$\dot{m}=\begin{cases}C_{vap}\alpha_v^2(1-\alpha_v)^2\dfrac{\rho_l}{\rho_v}\dfrac{p_v-p}{\sqrt{2\pi R_{gas}T_l}}, & \text{if } p<p_v\\ C_{con}\alpha_v^2(1-\alpha_v)^2\dfrac{p-p_v}{\sqrt{2\pi R_{gas}T_l}}, & \text{else}\end{cases} \tag{12}$$

where C_{vap} and C_{con} are empirical constants for evaporation and condensation of water, α_v is vapour volume fraction. This model was adopted in the numerical method proposed by [83] and applied to CFD simulations of liquid hydrogen cavitating flow around a hydrofoil in a tunnel [84], where the cavitation model Eq.(12) is modified into the following form

$$\dot{m}=\begin{cases}C_{vap}[\alpha_v(1-\alpha_v)]^{2/3}\dfrac{p_v-p}{\sqrt{2\pi R_{gas}T_l}}, & \text{if} p<p_v\\ C_{con}[\alpha_v(1-\alpha_v)]^{2/3}\dfrac{p-p_v}{\sqrt{2\pi R_{gas}T_l}}, & \text{else}\end{cases} \tag{13}$$

Additionally, the compressible viscous two-phase mixture flow model in [81,82] was updated in [85] by considering and including dissolved non-condensable gas. The cavitation inception process in a nozzle was then investigated with the model based on large eddy simulation (LES).

Another simplification of Eq.(10) can be found in [86], and the corresponding mass transfer rates are listed as the following

$$\dot{m}=\begin{cases}C_{vap}\dfrac{3(1-\alpha_v-\alpha_g)}{R}\sqrt{\dfrac{M}{2\pi R_{gas}T_l}}(p_v-p), & \text{if} p<p_v\\ C_{con}\dfrac{3\alpha_v}{R}\sqrt{\dfrac{M}{2\pi R_{gas}T_l}}(p_v-p), & \text{else}\end{cases} \tag{14}$$

where α_g is the volume fraction of the non-condensable gas in water, R is the vapour bubble radius. Eq.(14) was applied to CFD simulation of unsteady cavitating flows around a hydrofoil when$\alpha_g=0$ was held and the thermodynamic effect on R was considered [87,88]. Note that the model in Eq.(12) or (14) is for water only.

2.2.4. Rayleigh-Plesset equation-based mass transfer rate models

Rayleigh-Plesset equation-based mass transfer rate models are the cavitation models that are derived explicitly from the Rayleigh-Plesset equation for vapour bubbles. The first Rayleigh-Plesset equation-based mass transfer rate model was established by [89]. In the model, vapour bubbles are spherical, and in uniform size without interaction between them, and flow with the liquid at the same velocity. The vapour volume fraction α_v is defined in a mesh cell, and expressed as [89]

$$\alpha_v=\frac{n_0\frac{4}{3}R^3}{1+n_0\frac{4}{3}R^3} \tag{15}$$

where n_0 is the number of vapour bubbles in a unit volume, R is the radius of the bubbles. The vapour mass transfer rate is then calculated with the following equation [89]

$$\frac{d\alpha_v}{dt}=\left(\frac{n_0}{1+n_0\frac{4}{3}R^3}\right)\frac{d}{dt}\left(\frac{4}{3}R^3\right)=\left(\frac{n_0 4\pi R^2}{1+n_0\frac{4}{3}\pi R^3}\right)\frac{dR}{dt} \tag{16}$$

The general Rayleigh-Plesset equation which governs the dynamics of a spherical vapour bubble in an infinite body of incompressible fluid is written as [90]

$$R\frac{d^2R}{dt^2}+\frac{3}{2}\left(\frac{dR}{dt}\right)^2=\frac{p_v+p_g-p}{\rho_l}-\frac{4\nu}{R}\frac{dR}{dt}-\frac{2\gamma}{\rho_l R} \tag{17}$$

where p is the liquid pressure outside the vapour bubble, γ is the liquid surface tension, and ν is the liquid kinematic viscosity. p_g is the partial pressure of non-condensable gas in the bubble. After the 2nd-order term, surface tension, liquid viscosity and non-condensable gas are ignored, the bubble radius growth rate dR/dt should be determined by the following equation

$$\frac{dR}{dt}=\sqrt{\frac{2}{3}\frac{p_v-p}{\rho_l}} \tag{18}$$

Putting Eqs.(16) and (18) together, the cavitation model is derived as follows [89]

$$\frac{d\alpha_v}{dt}=\left(\frac{n_0}{1+n_0\frac{4}{3}\pi R^3}\right)\frac{d}{dt}\left(\frac{4}{3}R^3\right)=\left(\frac{n_0 4\pi R^2}{1+n_0\frac{4}{3}\pi R^3}\right)\sqrt{\frac{2}{3}\frac{p_v-p}{\rho_l}} \tag{19}$$

However, Eq.(16) is incorrect because the term $n_0\frac{4}{3}\pi R^3$ in the denominator has been neglected when the first derivative of Eq.(15) was taken with respect to t. Fortunately, the expression for the derivative was corrected by the same group in [91], and is presented in the following equation

$$\frac{d\alpha_v}{dt}=(1-\alpha_v)\left[\frac{n_0 4\pi R^2}{\left(1+n_0\frac{4}{3}\pi R^3\right)^2}\right]\frac{dR}{dt}=\frac{3\rho_l}{\rho}\frac{(1-\alpha_v)\alpha_v}{R}\sqrt{\frac{2}{3}\frac{p_v-p}{\rho_l}} \tag{20}$$

The corresponding vapour volume fraction transport equation is as the following

$$\frac{\partial(\alpha_v\rho_v)}{\partial t}+\frac{\partial(\alpha_v\rho_v u_i)}{\partial x_i}=\frac{3\rho_v\rho_l}{\rho}\frac{(1-\alpha_v)\alpha_v}{R}\sqrt{\frac{2}{3}\frac{p_v-p}{\rho_l}} \tag{21}$$

where the vapor bubble radius is determined from Eq.(15) with the known α_v and n_0, $R=\sqrt[3]{3\alpha_v/[4\pi n_0(1-\alpha_v)]}$. This is the known Schnerr-Sauer cavitation model. The cavitation model in Eq.(21) has been embedded in Fluent 6.1 and in STAR-CCM + .

Eq.(21) was modified with temperature-dependent thermophysical property constants and convective heat transfer model, the corresponding energy equation was solved to consider the thermodynamic effect in cavitation [92–97].

A notable updated version of the cavitation model Eq.(21) was presented in [98], where the second-order derivative and liquid surface tension terms in the Rayleigh-Plesset equation remain to derive dR/dt expression, namely

$$\frac{dR}{dt}=\sqrt{\left|\left(\frac{2}{3}\frac{p_v-p}{\rho_l}\right)\left(1-\frac{R_0^3}{R^3}\right)-\frac{2\gamma}{\rho_l R}\left(1-\frac{R_0^2}{R^2}\right)\right|} \tag{22}$$

From Eq.(15), the R in Eq.(21) is expressed with α_v by

$$R=\sqrt[3]{\frac{3}{n_0 4\pi}\frac{\alpha_v}{1-\alpha_v}} \tag{23}$$

Then, Eq.(21) was updated in the follow form

$$\begin{cases}\dfrac{\partial(\alpha_v\rho_v)}{\partial t}+\dfrac{\partial(\alpha_v\rho_v u_i)}{\partial x_i}=3.3\sqrt[3]{n_0\pi}\dfrac{\rho_v\rho_l}{\rho}\iota\sqrt[2]{|\zeta|}\,\mathrm{sign}(\zeta)\\ \iota=(1-\alpha_v)^2(n_0\xi)^{2/3},\ \xi=\dfrac{\alpha_v}{n_0(1-\alpha_v)}\\ \zeta=\left(\dfrac{2}{3}\dfrac{p_v-p}{\rho_l}\right)\left(1-\dfrac{4R_0^3}{\xi}\right)-\dfrac{3\gamma}{\rho_l\sqrt[3]{\xi}}\left(1-\dfrac{2.5R_0^2}{\sqrt[3]{\xi^2}}\right)\end{cases} \tag{24}$$

where R_0 is the initial radius of vapour bubbles. This model was applied to simulate unsteady cavitating flow over 2D hydrofoils [98]. The simplified version of Eq.(22) without liquid surface tension term can be found in [99,100]. Actually, Eq.(22) was derived in [101] as early as in the 1970′s.

Interestingly, based on the hydrodynamic similarity of cavitation, n_0 varies with the pressure difference p_v-p_{min} [102], namely

$$n_0=n_*\left(\frac{p_v-p_{min}}{p_v}\right)^{3/2} \tag{25}$$

where p_{min} is the minimum pressure in the throat of a nozzle considered, n_* is the number of vapour bubbles at$p_{min}=0$.

In [103], the second Rayleigh-Plesset equation-based mass transfer rate model, called full cavitation model, was devised for isothermal cavitation. The vapour mass fraction transport equation, where the cavitation model was attached as source term, was solved. The derivation process of the model is essentially similar to the Schnerr-Sauer cavitation model, Eq.(20), but there are a few differences, such as:

(1) $\alpha_v=n_0\frac{4}{3}\pi R^3=y\rho/\rho_v$, $1/\rho=y/\rho_v+(1-y)/\rho_l$, y is vapour mass fraction;
(2) the vapour bubble radius is determined by the balance between aerodynamic drag and surface tension found in the literature;
(3) non-condensable gas/air in the liquid is taken into account.

Additionally, the mass transfer/change rate was developed in an approximate manner. The following is the vapour mass fraction transport equation during bubble growth or condensation [103]

$$\frac{\partial(\alpha_v\rho_v)}{\partial t}+\frac{\partial(\alpha_v\rho_v u_i)}{\partial x_i}=\dot{m} \tag{26}$$

where u_i are fluid velocity components in the Cartesian coordinate system, x_i are the Cartesian coordinates in a flow field, i=1,2,3, which are the coordinate index, $\dot{m}$ is cavitation mass transfer rate, considered as the product of vapour density and velocity divergence, namely $\dot{m}=\rho_v\partial u_i/\partial x_i$. The continuity equation of the vapour and liquid mixture in non-conservative form is employed to determine $\dot{m}$:

$$\frac{\partial\rho}{\partial t}+\frac{\partial(\rho u_i)}{\partial x_i}=\frac{d\rho}{dt}+\rho\frac{\partial u_i}{\partial x_i}=0 \tag{27}$$

where ρ is the density of the mixture, $\rho=\alpha_v\rho_v+(1-\alpha_v)\rho_l$. From Eq.(27), the velocity divergence can be expressed with $d\rho/dt$ as such

$$\frac{\partial u_i}{\partial x_i}=-\frac{1}{\rho}\frac{d\rho}{dt} \tag{28}$$

Since

$$\frac{d\rho}{dt}=\frac{d}{dt}[\alpha_v\rho_v+(1-\alpha_v)\rho_l]=(\rho_v-\rho_l)\frac{d\alpha_v}{dt} \tag{29}$$

Then, we have

$$\dot{m}=\rho_v\frac{\partial u_i}{\partial x_i}=\rho_v\left(-\frac{1}{\rho}\frac{d\rho}{dt}\right)=\rho_v\frac{(\rho_l-\rho_v)}{\rho}\frac{d\alpha}{dt}\approx\frac{\rho_v\rho_l}{\rho}\frac{d\alpha_v}{dt} \tag{30}$$

where the term ρ_v^2 has been neglected.

Because of $d\alpha_v/dt=d\left(n_0\frac{4}{3}\pi R^3\right)\Big/dt=\left(n_0 4\pi R^2\right)dR/dt$, the vapour volume fraction transport equation Eq.(26) is rewritten as

$$\frac{\partial(\alpha_v\rho_v)}{\partial t}+\frac{\partial(\alpha_v\rho_v u_i)}{\partial x_i}=(n_0 4\pi)^{1/3}(3\alpha_v)^{2/3}\frac{\rho_v\rho_l}{\rho}\sqrt{\frac{2}{3}\frac{p_v-p}{\rho_l}} \tag{31}$$

or

$$\frac{\partial(\alpha_v\rho_v)}{\partial t}+\frac{\partial(\alpha_v\rho_v u_i)}{\partial x_i}=\frac{3\alpha_v}{R}\frac{\rho_v\rho_l}{\rho}\sqrt{\frac{2}{3}\frac{p_v-p}{\rho_l}} \tag{32}$$

Note that Eq.(32) serves as the working transport equation in [102]. The vapour bubble radius R varies in both evaporation and condensation. However, it was treated with a constant that is proportional to the ratio of the liquid surface tension to the relative velocity between bubbles and liquid. This can be a flaw of the model. If Eq.(31) is adopted in the model, R will not appear explicitly in the equation.

Eq.(31) was adopted in the cavitation model in [104]. In this case, the vapour bubble radius R no longer emerges explicitly in the model, thus the flaw disappears. Moreover, the energy equation was activated to allow the thermodynamic effect in cavitation to be considered.

That flaw was tackled in [105] as well by making use of $R\propto 1/|p_v-p|$. Furthermore, the vapour pressure was reduced by subtracting the pressure depression Δp_v of B factor related to allow the model to deal

with cavitation with thermodynamic effect. In this case, the energy equation does not need to be activated and the liquid thermophysical property constants are assumed to be independent of temperature.

The classical thermodynamic phase-change theory was applied to determine vapour bubble R in Eq.(31), the energy equation was activated and temperature-dependent thermophysical property constants were input into Fluent to include the thermodynamic effect in cavitation [106].

The thermophysical property constants of liquid in the original full cavitation model were changed into temperature-dependent and the energy equation was solved in Fluent to predict the thermodynamic effect in cavitation [107,108].

In [109], the third Rayleigh-Plesset equation-based mass transfer rate model, called ZGB cavitation model, was proposed. Actually, it is a simplified version of the full cavitation model for isothermal cavitation. For convenience, one of the phasic continuity equations was derived as the sum of the liquid and vapour continuity equations divided by their individual densities as follows:

$$\frac{1}{\rho_v}\left[\frac{\partial(\alpha_v\rho_v)}{\partial t}+\frac{\partial(\alpha_v\rho_v u_i)}{\partial x_i}-\dot{m}_v\right]+\frac{1}{\rho_l}\left\{\frac{\partial[(1-\alpha_v)\rho_l]}{\partial t}+\frac{\partial\left[(1-\alpha_v)\rho_l u_i\right]}{\partial x_i}-\dot{m}_l\right\}=0 \tag{33}$$

where $\dot{m}_v$ is the vapour mass transfer rate, $\dot{m}_l$ is the liquid mass transfer rate, particularly,$\dot{m}_v = -\dot{m}_l = \dot{m}$. Eq.(33) can then be rewritten as

$$\frac{1}{\rho_v}\left[\frac{\partial(\alpha_v\rho_v)}{\partial t}+\frac{\partial(\alpha_v\rho_v u_i)}{\partial x_i}\right]+\frac{1}{\rho_l}\left\{\frac{\partial[(1-\alpha_v)\rho_l]}{\partial t}+\frac{\partial\left[(1-\alpha_v)\rho_l u_i\right]}{\partial x_i}\right\}=\dot{m}\left(\frac{1}{\rho_v}-\frac{1}{\rho_l}\right) \tag{34}$$

where the right-hand side source term should be equal to Eq.(28). In this context, the following equation should be held

$$\dot{m}\left(\frac{1}{\rho_v}-\frac{1}{\rho_l}\right)=\frac{\partial u_i}{\partial x_i}=-\frac{1}{\rho}\frac{d\rho}{dt}=\frac{(\rho_l-\rho_v)}{\rho}\frac{d\alpha_v}{dt} \tag{35}$$

Finally, the vapour mass transfer rate $\dot{m}$ can be expressed in the following form

$$\dot{m}=\frac{\rho_l\rho_v}{\rho}\frac{d\alpha_v}{dt} \tag{36}$$

This expression is the same as Eq.(30). Therefore, the vapour volume fraction transport equation is the same as Eq.(31) or (32). The ZGB cavitation model shares the same physical basis as the full cavitation model, and it is one simplified version of the latter.

Substituting $d\alpha_v/dt = \left(n_0 4\pi R^2\right)dR/dt$ into Eq.(36), the vapour mass transfer rate is related to $p_v - p$ as follows

$$\dot{m}=\frac{\rho_l\rho_v}{\rho}\frac{3\alpha_v}{R}\sqrt{\frac{2}{3}\frac{p_v-p}{\rho_l}} \tag{37}$$

Eq.(37) is applicable to vapour condensation directly. However, owing to the simplification of $\alpha_v = n_0\frac{4}{3}\pi R^3$, it fails to reflect the fact that the nucleation site density will decrease during evaporation with increasing α_v. Thus, Eq.(37) has to be modified with $1-\alpha_v$ for the evaporation

$$\dot{m}=\frac{\rho_l\rho_v}{\rho}\frac{3\alpha_{nc}(1-\alpha_v)}{R}\sqrt{\frac{2}{3}\frac{p_v-p}{\rho_l}} \tag{38}$$

where α_{nc} is the nucleation site volume fraction in liquid. Considering $\rho_l \approx \rho$ and R=R_0 = constant in cavitation, the following form comes for the ZGB cavitation model

$$\dot{m}=\begin{cases}F_{vap}\dfrac{3\alpha_{nc}(1-\alpha_v)\rho_v}{R_0}\sqrt{\dfrac{2}{3}\dfrac{p_v-p}{\rho_l}}, & \text{if } p<p_v\\[2ex] F_{con}\dfrac{3\alpha_v\rho_v}{R_0}\sqrt{\dfrac{2}{3}\dfrac{p-p_v}{\rho_l}}, & \text{else}\end{cases} \tag{39}$$

where F_{vap} and F_{con} are empirical constant, R_0 is the initial radius of vapour bubbles or the radius of nucleation sites. In ANSYS CFX, the default values of these model constants are: F_{vap}=50, F_{con}=0.01, R_0=10^{-6}m, α_{nc}=5×10^{-4} for isothermal cavitation of water.

The ZGB cavitation model has been extended into the cavitation modelling with thermodynamic effect. There are two methods for taking the thermodynamic effect into account. The first method is dR/dt correction, while the second method uses temperature-dependent thermophysical property constants. In the first method, the unsteady [110–114] or steady [115–117] heat transfer equation is established in the interface between a spherical vapour bubble and the liquid to calculate dR/dt correction caused by liquid temperature depression. Additionally, the thermophysical property constants in the model are changed into temperature-dependent state, and the energy equation is activated. The model empirical factors F_{vap} and F_{con} are calibrated against experimental data of cavitation with thermodynamic effect. In the second method, the thermophysical property constants in the model are changed into temperature-dependent state, and the energy equation is solved to calculate temperature field in the fluid domain along with calibrated factors F_{vap} and F_{con} [118–121].

Later, the so-called unified cavitation model, i.e., the fourth Rayleigh-Plesset equation-based mass transfer rate model, was proposed in [122]. The model can be simplified to Eqs.(9), (21), (32) and (37), respectively, when its right hand side term is assigned with different coefficients and exponents.

2.2.5. Nucleation cavitation models

Experimental observations have suggested that cavitation is initiated by foreign gas or solid particles (cavitation nuclei) with a spectrum of 10–200 μm size in a liquid, as documented in the literature since the 1970′s [123–128]. These observations indicate that cavitation should involve a nucleation mechanism of nuclei in different sizes.

Cavitation nuclei have been taken into account in cavitating flow modelling as cavitating clouds with a nuclei number density distribution function since the 1990′s. There are four types of cavitation models to tackle cavitation nucleation, including:

(1) empirical function of nuclei number density distribution with the Rayleigh-Plesset equation but without thermodynamic effect;
(2) vapour nucleation theory with the Rayleigh-Plesset equation;
(3) vapour nucleation theory with empirical function of nuclei number density distribution;
(4) vapour nucleation theory with existing simplified cavitation models in CFD package.

In the first nucleation cavitation model as listed above, the experimental spectrum of 10–200 μm of gas nuclei was best fitted by using the following empirical function in terms of three constants and one power function of initial nuclei size R_0

$$\chi(R_0)=\frac{3\alpha_0}{4\pi(1-\alpha_0)ln(R_{0max}/R_{0min})R_0^m} \tag{40}$$

where α_0 is the initial nuclei volume fraction, m is the empirical power, m=3.5 [128], or$m$ = 4.0 [129]; R_{0max} and R_{0min} are the maximum and minimum initial nuclei sizes, respectively. Based on Eq.(40), the number of nuclei per unit liquid volume with initial size between R_0 and$R_0 + dR_0$ is $\chi(R_0)dR_0$, the Rayleigh-Plesset equation for single vapour bubble without thermodynamic effect was modified. The response behaviour of

a vapour bubble cloud to transient pressure was clarified in [129]. Similarly, when a vapour bubble cloud flows through an artificial convergent-divergent nozzle, the vapour bubble growth and collapse properties were investigated numerically [130].

The second nucleation cavitation model was given by [127] based on experimental data. The nuclei size profile was best fitted with an exponential function and three model constants. Since there are more model constants underdetermined, this model is inconvenient in applications.

The vapour nucleation theory was proposed in the 1920′s to deal with the vapour bubble growth when the vaporization of liquid molecules at the interface into the bubble is taking place. In the theory, the vaporization of liquid molecules is decided by vapour bubble nucleation rate, i.e., the population of vapour bubbles in critical size in the liquid. The vapour bubble critical size is related to the minimum work needed to create a vapour bubble, which includes the work to create the bubble surface and the maximum work done by the expanding vapour. The minimum work can be calculated with the bubble mechanical equilibrium equation, i.e., the Rayleigh-Plesset equation without transient and viscous terms. The population of vapour bubbles in critical size is assumed to be an exponential function of the work [131]

$$N = N_l exp(-W/\kappa T_l) \tag{41}$$

where N_l is the population density of impurity particles or seeding nuclei in the liquid, W is the minimum work, κ is the Boltzmann constant. For homogeneous (spherical) vapour bubbles and heterogeneous vapour bubble (lens-shaped or partially spherical or conical cavity/bubble fixed on wall), $W/\kappa T_l$ is the normalized Gibbs activation energy [132]. The population of vapour bubbles in critical size is written as [133,134]

$$N = N_l^{2/3}\left(\frac{1-\cos\theta}{2}\right)\left(\frac{2\gamma}{\pi\delta a\cos\theta}\right)^{1/2} exp\left(-\frac{16\pi\gamma^3\delta}{3\kappa T_l(p_v-p_l)^2}\right) \tag{42}$$

where θ is the half angle of the bubble surface measured at the centre of the surface curvature, δ is a geometrical parameter depending on vapour bubble shape, $\delta = (2-3\cos\theta+\cos^3\theta)/4$, a is constant, γ is liquid surface tension, p_v is vapour pressure, p_l is the liquid pressure outside the bubble. Molecular dynamics simulations of the Lennard–Jones fluid under negative pressure were performed in [135] to calculate nucleation rate when cavitation occurred by reducing liquid pressure, it was shown that the predicted cavitation nucleation rate was larger than that estimated with Eq.(42) by eight orders, suggesting that Eq.(42) should be used carefully in cavitation inception prediction.

Recently, the classical theory of vapour bubble was advanced in [136–138] by considering surface energy of liquid molecule clusters, thermodynamics and nucleation kinetics of the clusters. The proposed nucleation rate of vapour bubbles is written as [138]

$$N = N_l D_n Z_f exp\left(-\frac{W_{min}}{\kappa T_l}\right) \tag{43}$$

where D_n is the rate that molecules strike the surface of the clusters with n molecules, Z_f is the Zeldovich non-equilibrium factor, $Z_f = \sqrt{(-1/2\pi\kappa T_l)\left[\partial^2 W_{min}/\partial n^2\right]}$, the minimum work W_{min} is related to the cut-off distance characteristic l_c at zero surface tension (critical point), the number of nearest neighbouring molecules surrounding a single molecule z, $W_{min} = zl_c n^{2/3}/6$. The detailed formulas for N can be found in [136–140] and thus are omitted here. It should be noted that this model is a homogeneous model for spherical vapour bubble in a liquid. In this context, it was applied to analyse a laser-induced cavitation problem by combining it with the governing equations of fluid and heat flows around bubbles [139].

The third cavitation model is based on the vapour nucleation theory with the Rayleigh-Plesset equation. In this model, the classical nucleation theory expressed with Eq.(42) is introduced into the vapour bubble mass conservation equation as a source term, and it is solved along with the Navier-Stokes equations and Rayleigh-Plesset equation as well as conductive heat transfer equation. As a result, the cavitating flows with thermodynamic effect were tackled [140–143]. A similar but one-dimensional (1D) cavitating flow with the classical nucleation theory without thermodynamic effect was treated in [144], where the non-condensable gas was considered.

In the fourth nucleation cavitation model, the empirical function of nuclei number density distribution Eq.(40) and vapour nucleation theory expressed Eq.(42) are combined, and the non-condensable gas concentration and partial pressure are considered as well. The mass transfer rates are similar to the ZGB model [145].

In the fifth nucleation cavitation model, the vapour nucleation theory is expressed with Eq.(42). The nucleation rate of the water flow through a divergent-convergent nozzle was simulated in Fluent solver with user-defined function (UDF) subroutine [146]. The UDF subroutine handles Eq.(42) and solves the bubble mass conservation equation by using the quadrature method of moments. In fact, the cavitation model in Fluent was not activated [146]. In [147,148], the nucleation theory with Eq.(42) or (43) was coupled with the Schnerr-Sauer cavitation model with vapour volume fraction. Once again, the bubble mass conservation equation was solved with the quadrature method of moments and thermodynamic effect was included in the energy equation. These equations were simulated along with the Navier-Stokes equations and $k-\omega$ turbulence model in an open-source code-OpenFOAM Version 3.01.

2.3. Multiscale models

Vapour bubble inception and collapse are critical in cavitation since they are relevant to cavitation occurrence and cavitation damage to a solid wall. Bubble inception and collapse are in microscale actually, but also affected by the local macroscale flow field around a hydrofoil or in an impeller. Typically, cavitating flows are multiscale problems in physics.

For cavitation inception, a one-way multiscale cavitation model was developed in [149–152]. In the model, the macroscale incompressible flow in or around a device is known in advance based on experimental measurement [149,150] or analytical solution of a Rankine vortex [151] or Lamb-Oseen vortex [152]. A number of spherical nuclei are then released at the inlet to the flow field and their trajectory is tracked by using the Corrsin and Lumley equations of motion of particles [153] with the obtained flow field information. In the meantime, the bubble radius is estimated by means of the Rayleigh-Plesset equation to identify bubble location and size. This is the initial one-way multiscale cavitation inception model. Currently, the model is updated by using the macroscale incompressible turbulent flow field which was obtained by solving the Reynolds time-averaged Navier-Stokes Equations [154–157].

Vapour bubble collapse near a solid boundary may occur in a stationary or flowing liquid. In the former case, e.g., ultrasound-induced cavitation, the liquid is still and its flow during bubble collapse can be considered as potential flow around a bubble. The bubble deformation in the collapse is treated with the boundary element method and the Rayleigh-Plesset equation, as summarised in an existing review [158]. Recently, the bubble or its cloud collapse in a stationary liquid (computational domain is in a few mm^2 area or a few mm^3 volume) is modelled with compressible homogeneous two-phase flow models proposed by [81], for example, those in [159–162] or the flow model by using a high-order accurate shock- and interface-capturing scheme [163,164]. A systemic review of this issue is devoted to [165].

When vapour bubble collapse appears near a boundary in a flow system, the equations of motion and Rayleigh-Plesset equation for bubbles were involved in the compressible homogeneous two-phase flow models in [81] to form a one-way multiscale fully developed cavitation model [166]. The transient liquid pressure applied to the hydrofoil wall by the bubbles during their collapse was captured.

This model was expanded to estimate cavitation damage rate to a wall when bubbles collapse near the wall in [82,167]. To achieve this goal, the collapse process of a spherical bubble near the wall was analysed based on the model proposed by [168], where the bubble yielded the Rayleigh-Plesset equation and the liquid around the bubble was compressible and spherically symmetrical and described with a potential function. In [169], the homogeneous incompressible turbulent two-phase mixture flow in a nozzle was calculated by using the known Schnerr-Sauer cavitation model, then a series of bubbles was released at the nozzle inlet, the bubble trajectories were determined by making use of the equations of motion of bubbles, and the bubble sizes were calculated by means of the Rayleigh-Plesset equation. The impact pressure generated by bubble collapse was predicted with the method in [170]. Finally, the cavitation erosion rate was simply estimated with the impact pressure. Once again, these are one-way multiscale cavitation models.

A few multiscale or Euler-Lagrange fully coupled cavitation models were developed in [171–178]. In the first multiscale cavitation model proposed in [171], the cavitating bubbles are spherical with uniform radius locally and are separated without interactions between the bubbles or between the bubbles and the liquid phase. The number of bubbles is in conservation as well. There is no slip between the bubbles and the liquid. The radius of the bubbles in a mesh cell yields the unsteady Rayleigh-Plesset equation without liquid surface tension, viscosity damping effect and non-condensable gas under isothermal condition. The Rayleigh-Plesset equation, Navier-Stokes equations and pressure Poisson's equation were coupled in the numerical procedure.

Note that the multiscale cavitation model in [173] has been the most advanced model because the vapour bubble breakup and coalescence have been considered.

A four-way coupled multiscale cavitation model was reported by using a variational multiscale method preliminarily and the bubble interaction is modelled with a soft sphere contact model in [176]. This seems to be a promising model for simulating cavitation in future.

In the multiscale cavitation modelling method described in [178], cavitating flows can be treated as multiscale problems. The multiscale is at three levels such as macroscale, microscale, and inter-scale in between. The macroscale cavitating flow represents large bubbles, cavities and air pockets in a flow field and is handed with ordinary continuum-based phase averaged two-phase mixture flow model along with a level set method. The mixture flows are described by the incompressible Navier-Stokes equations and the level set method is employed to capture the interfaces between the cavities and the liquid. The microscale flow is discrete vapour bubbles. The motion of a bubble is determined by solving the equation of motion of the bubble and the pressure inside the bubble is calculated by using the Rayleigh-Plesset equation updated with a term of the relative velocity of the bubble to the liquid. The inter-scale flow reflects bubble merging, shrinking and breaking up, which is decided by using information from the macroscale and microscale solutions. Since the solutions in the macroscale and microscale should be coupled, this multiscale cavitation model is two-way coupling and very time-consuming, and might be hard in applications. Additionally, the interaction between bubbles doesn't seem to be involved in the model.

Very recently, a simple version of the multiscale model was proposed in [179]. The macroscale flow field is simulated with the incompressible Navier-Stokes equations, shear stress transport (SST) turbulence model and Schnerr–Sauer cavitation model. The cavity shape is calculated by using volume of fluid (VOF) method. The vapour bubble size is tracked by employing a discrete bubble model (DBM) in the Lagrange formulation in the known pressure field just obtained in the macroscale simulation. The simplified Rayleigh-Plesset equation without liquid viscosity, surface tension, non-condensable gas and term Rd^2R/dt^2 is used to calculate uniform individual bubble radius in the DBM. Basically, this is one-way coupling multiscale cavitation model only.

A multiscale cavitation model was developed to predict erosion due to cavitation in [180]. It can capture large scale vapour volume in the Eulerian reference frame and treat small scale vapour volume as spherical bubbles in the Lagrange reference frame. Interactions between the vapour bubbles and the liquid phase are handled with a two-way coupling scheme.

3. Implementation of thermodynamic effect

3.1. Vapour bubble growth rate

The thermodynamic effect on growth and collapse of vapour bubbles has been concerned since the 1930's based on the Rayleigh-Plesset equation and conductive heat transfer equation for phase change [181–192]. In these studies, spherical vapour bubbles were considered, the Rayleigh-Plesset equation was linearised with the Clausius-Clapeyron relation, then coupled with the 1D conductive heat transfer equation to obtain the asymptotic growth rate of vapour bubble radius under various thermodynamic conditions. A comprehensive review of this subject is referred to [193].

Recently, these equations are solved numerically to cover a wide range of Jakob number [194–197]. The Jakob number J is defined as the ratio of the sensible heat to the heat absorbed for evaporation and expressed by [195]

$$J = \frac{\rho_l c_{pl}(T_l - T_v(p))}{\rho_v L} \tag{44}$$

where c_{pl} is liquid specific heat, T_l and p are liquid temperature and static pressure in far-field, $T_v(p)$ is liquid saturation boiling temperature at p, L is the latent heat of evaporation of liquid, the temperature difference $T_l - T_v(p)$ reflects the superheat generated artificially in the fluid field. For hydrodynamic cavitation, there is no superheat provided, $T_l - T_v(p)$ should be replaced with the local difference of the liquid temperature T_l from the vapour temperature T_v, i.e., $T_l - T_v$.

Based on Eq.(17), the Rayleigh-Plesset equation with neglected liquid viscosity, surface tension and non-condensable gas for a spherical vapour bubble with radius R in an incompressible liquid is written as [195]

$$R\frac{d^2R}{dt^2} + \frac{3}{2}\left(\frac{dR}{dt}\right)^2 = \frac{p_v - p}{\rho_l} - \frac{2\gamma}{\rho_l R} \tag{45}$$

where γ is liquid surface tension. In the equilibrium state, the unsteady term Rd^2R/dt^2 and inertial term dR/dt vanish, the bubble is in equilibrium between the surface tension and the transmural pressure with the equilibrium radius $R_0 = 2\gamma/(p_v - p)$ by the Young-Laplace equation. Eq. (45) has two analytic asymptotic solutions under two conditions: (1) inertia controlled bubble growth; and (2) heat-diffusion controlled bubble growth.

Under the inertia controlled growth condition, the unsteady term $Rd^2R/dt^2$and surface tension γ are assumed to be zero, and the solution of Eq.(45) has been expressed by Eq.(18), which had been applied in the existing cavitation models. The Clausius-Clapeyron relation at a point close to the saturation point of a liquid reads as

$$\frac{p_v - p}{T_v - T_l} \approx \frac{dp_v}{dT_l} \approx \frac{L\rho_v}{T_l} \tag{46}$$

After the difference $p_v - p$ is substituted with Eq.(46), the vapour bubble growth rate is as a function of liquid thermodynamic parameters such as

$$\frac{dR}{dt} = \sqrt{\frac{2}{3}\frac{T_v - T_l}{\rho_l}\frac{L\rho_v}{T_l}} \tag{47}$$

Eq.(47) demonstrates that if p_v is expressed as a function of T_l and the heat transfer is coupled, the cavitation models Eq.(18) can cope with the thermodynamic effect in cavitation as long as their empirical constants have been calibrated properly with sufficient experimental data.

Under the heat-diffusion control condition, the vapour bubble growth is fully controlled by superheat. In 1930, Bosnjakovic proposed a model of vaporization process at uniform superheat. The temperature drop across a vapour bubble boundary occurs suddenly in a thin boundary layer which surrounds the bubble. Based on the energy balance, a relation between the bubble growth rate, the temperature drop, and the heat transfer coefficient is obtained as follows [186]

$$L\rho_v\frac{dR}{dt}=h(T_l-T_v) \tag{48}$$

where h is heat transfer coefficient across the bubble boundary. Unfortunately, this equation was not coupled with Eq.(45) to look for the vapour bubble growth rate.

Instead, the 1D conductive heat transfer equation, i.e. the energy balance equation in the liquid around a vapour bubble, which is written as the following form in a spherical coordinate system, was coupled with Eq.(45) along with proper initial and boundary conditions on the vapour bubble boundary and in the far-field:

$$\rho_l c_{pl}\frac{\partial T_l}{\partial t}=\lambda\frac{1}{r^2}\frac{\partial}{\partial r}\left(r^2\frac{\partial T_l}{\partial r}\right) \tag{49}$$

where λ is liquid thermal conductivity, r is the radial coordinate of the spherical coordinate system. The general solutions of vapour bubble growth rate are complex and cannot be expressed analytically. After they are simplified, the leading term of the growth rate is in the simplest form [186]

$$L\rho_v\frac{dR}{dt}=\frac{b\lambda}{\sqrt{\pi\mathscr{D}t}}(T_l-T_v) \tag{50}$$

where $\mathscr{D}$ is thermal diffusivity of liquid, b is solution constant, e.g., $b=\sqrt{3}$ [181], $\pi/2$ [190]. It is found that $b=\pi/2$ can better fit the experimental data [186].

Eqs.(47) and (50) provide the vapour bubble growth rates in the two extreme cases only. The vapour bubble growth rate between the extreme cases was worked out in [188], and the corresponding dimensionless vapour bubble radius R^+ is written as

$$\begin{cases} R^+=\dfrac{2}{3}\left[(t^++1)^{3/2}-(t^+)^{3/2}-1\right] \\ R^+=Rv/\psi^2,\ t^+=tv^2/\psi^2 \\ v^2=\dfrac{2L\rho_v(T_l-p_v)}{3\rho_l T_v(p)},\ \psi=(12\mathscr{D}/\pi)^{1/2}J \end{cases} \tag{51}$$

Eqs.(47) and (50) can be integrated with respect to time t, then are written as a function of R^+ and t^+, yielding Eq.(51), as shown in Fig. 5. It is seen that Eq.(51) fills the gap between two extreme cases properly. Eq.(47) for the inertia-controlled condition will overpredict the vapour bubble radius growth rate under the superheat-controlled condition; while Eq.(50) will underpredict it. Since Eq.(51) is valid in various thermal conditions, it potentially can be adopted in a cavitation model in future.

3.2. Methods for implementing thermodynamic effect

The methods for implementing thermodynamic effect in existing cavitation models are listed in Table 2. The first method is modifying the vapour pressure of liquid with its pressure depression Δp_v calculated by B-factor [105]. The B-factor was related to vapour volume fraction and temperature depression. The temperature depression depends on liquid temperature and thermophysical property constants only [198]. In this context, the energy equation is not needed, and the liquid thermophysical property constants can be independent of liquid temperature. The studies in [116,117] fall into this class, too.

The second method for implementing thermodynamic effect in the existing cavitation models related to Eq.(18) or (47) is allowing the vapour pressure, liquid and vapour specific heats etc to be a function of liquid temperature, while activating the energy equation to obtain the liquid and vapour temperature fields. Since Eq.(18) or (47) is for the inertia-controlled condition, the model constants in the existing cavitation models have to be calibrated to fit the experimental data associated with thermodynamic effect. The contributions in [36,72–78,92,93,96,106–108,118–121] belong to this category.

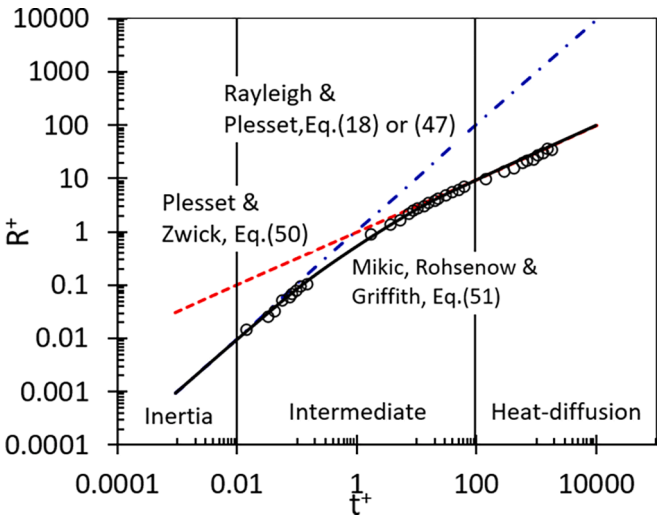

Fig. 5. Dimensionless vapour bubble radius R^+ is plotted as a function of dimensionless time t^+ for three bubble growth rate solutions, the symbols denote the test data.

The third method is an approach based on the correction of dR/dt. In this method, the vapour bubble growth rate calculated from Eq.(18) and the rate calculated from Eq.(50) are put together as an arithmetic sum, and the total growth rate is then adopted in the existing cavitation models. Additionally, the thermophysical property constants of the liquid and its vapour are made temperature-dependent and the energy equation is activated. The studies in [97,110–112] fall into this category. However, this method is questionable because the bubble growth rates calculated from Eq.(18) and Eq.(50) are in different cavitation regimes and cannot be simply put together.

The fourth method is an approach based on cavitation regime transition. In [199], a cavitation model for vapour bubble growth in a superheated liquid was developed. The vapour bubble growth rate is initially determined with Eq.(18) under the inertia-controlled condition, and it then goes into the superheat-controlled condition immediately without any intermediate cavitation regimes. The growth rate in the superheat-controlled condition was determined by the spherical vapour bubble growth rate proposed in [184]. It is the accurate asymptotic solution of the coupled equations of the Rayleigh-Plesset equation (without viscous, inertia, surface tension terms) with the conductive heat transfer equation in a binary solution and the heat balance equation Eq.(48). The heat transfer coefficient was calculated with the empirical correlations of Nusselt number in terms of Jakob number and Péclet number founded in the literature. The Péclet number accounts for the slip in velocity between the vapour bubble and the liquid. Since the model was not validated against any experimental data, the reliability and applicability of the model has been unknown so far.

In the fifth method, the Bosnjakovic evaporation model Eq.(48) is integrated with the Rayleigh-Plesset equation to form an updated Rayleigh-Plesset equation. The vapour bubble growth is then solved from the updated equation [104,115,198]. However, the heat transfer coefficient h around the vapour bubble becomes a model parameter inevitably. The effects of heat transfer coefficient on hydrogen cavitating flows in a venturi were investigated numerically and an optimal range of [105,106] was suggested for the heat transfer coefficient [200].

Although the vapour bubble growth rate due to the thermodynamic

Table 2
Thermodynamic effect implement in existing cavitation models.

Method	Contributor(year)	Feature	Source
B-factor method	Tsuda, Tani & Yamanishi (2012); Li, Yang, Shi et al (2018); Shao, Zhang & Zhou (2020)	1. Vapour pressure of liquid with its pressure depression Δp_v is calculated by *B*-factor directly. 2. Energy equation of fluid flow is no need to solve.	[105,116,117]
Temperature-dependent thermal properties	Hosangadi & Ahuja (2005); Shi &Wang (2012); Chen, Huang, Wang, et al. (215); Chen, Wang, Huang, et al. (215); Sun, Wei & Wang (2016); Tseng & Shyy (2010); Hosangadi, Ahuja & Ungewitter (2007); Zhang, Wu, Xiang, et al (2013); Zhao, Zhang & Shao (2011); Zhang, Qiu, Qi, et al (2008); Zhu, Chen, Zhao, et al (2015); Zhu, Zhao, Xu, et al (2016); Xue, Ruan, Liu X, et al (2017); Zhu, Wang, Qiu, et al (2018); Wang, Zhang, Hou, et al (2019); Song & Sun (2020); Xu, Feng, Wan, et al (2020); Li & Yu (2021)	1. Vapour pressure, liquid and vapour specific heats etc are a function of liquid temperature. 2. Energy equation of fluid flow is activated to gain liquid and vapour temperature fields.	[36,72–78,92,93,96,106–108,118–121]
Vapour bubble growth rate correction	Zhang, Luo, Ji, B et al (2010); Tang, Bian, Wang, et al (2013); Huang, Wu & Wang (2014); Liu, Li, Wang, et al (2020), Liu, Li, Lin, et al (2021)	1. Vapour bubble growth rates under inertia and heat-diffusion conditions are summed. 2. Thermophysical property constants of the liquid and vapour are temperature-dependent. 3. Energy equation is activated.	[97,110–112,114]
Cavitation regime transition	Colombet, Goncalvès Da Silva & Fortes-Patella (2017)	1. Vapour bubble growth rate is decided initially under inertia controlled condition, then under superheat-controlled condition. 2. Bosnjakovic evaporation model and Rayleigh-Plesset equation are coupled.	[199]
Combination of Bosnjakovic evaporation model and Rayleigh-Plesset equation	De Giorgi, Ficarella & Fontanarosa (2017), De Giorgi, Bello & Ficarella (2010); Zhang, Li & Zhu (2018); Franc & Pellone (2007)	1. Bosnjakovic evaporation model and Rayleigh-Plesset equation are coupled to have an updated Rayleigh-Plesset equation. 2. Solve the updated Rayleigh-Plesset equation for vapour bubble growth rate.	[95,104,115,198]

effect was calculated in [115], the rate was simply added to the growth rate determined by Eq.(18) rather than including the rate into the Rayleigh-Plesset equation to generate an updated Rayleigh-Plesset equation. Furthermore, the vapour pressure in Eq.(18) should be constant rather than a variable local pressure which has contributed to the Clausius-Clapeyron equation. Based on these two drawbacks, the model proposed in [115] is improper apparently.

The vapour bubble growth rate in Eq.(48) was used directly in the cavitation model without coupling with the Rayleigh-Plesset equation in [201]. The corresponding cavitation model was applied to predict the cavity of water at 21, 30 and 50℃ in a sharp-edged orifice. It was shown that the model underestimated the cavity length in comparison with the full cavitation model of [103].

Compared with the other cavitation models, the ZGB cavitation model is more widely applied to simulate cavitating flows and involve the thermodynamic effect.

3.3. Cavitation models with liquid viscosity

In all the cavitation models mentioned above, liquid viscosity has been ignored. The liquid viscosity varies with liquid temperature when the thermodynamic effect takes place in cavitation. In [202], based on the following simplified Rayleigh-Plesset equation

$$\frac{3}{2}\left(\frac{dR}{dt}\right)^2+\frac{4\nu}{R}\frac{dR}{dt}=\frac{p_v-p}{\rho_l} \tag{52}$$

where ν is kinematic viscosity of liquid. The vapour bubble growth rate is obtained as

$$\frac{dR}{dt}=\frac{1}{3}\left[\sqrt{6\frac{p_v-p}{\rho_l}+\left(\frac{4\nu}{R}\right)^2}-\frac{4\nu}{R}\right] \tag{53}$$

Finally, the ZGB cavitation model expressed by Eq. (39) is updated as follows after set $R=R_0$

$$\dot{m}=\begin{cases} F_{vap}\dfrac{\alpha_{nc}(1-\alpha_v)\rho_v}{R_0}\left[\sqrt{6\dfrac{p_v-p}{\rho_l}+\left(\dfrac{4\nu}{R_0}\right)^2}-\dfrac{4\nu}{R_0}\right], & \text{if } p\le p_v \\ F_{con}\dfrac{\alpha_v\rho_v}{R_0}\left[\sqrt{6\dfrac{p-p_v}{\rho_l}+\left(\dfrac{4\nu}{R_0}\right)^2}-\dfrac{4\nu}{R_0}\right], & \text{else} \end{cases} \tag{54}$$

The cavitating flows of water at 25, 70 and 150℃ around the NACA0015 hydrofoil were simulated in ANSYS CFX under the conditions of variable vapour saturation pressure, 5° angle of attach and a cavitation number of 1.5. The corresponding results agree with the experimental data, Unfortunately, the values of the model constants F_{vap} and F_{con} remain unknown [202].

A similar cavitation model with both liquid viscosity and thermodynamic effect is found in [203]. Similar to Eq.(52), the simplified Rayleigh-Plesset equation is expressed as [203]

$$\frac{3}{2}\left(\frac{dR}{dt}\right)^2+\frac{4\nu}{R}\frac{dR}{dt}=\frac{p_v(T_\infty)-p}{\rho_l} \tag{55}$$

here $p_v(T_\infty)$ is the vapour pressure based on the liquid temperature in the far-field. $p_v(T_\infty)-p$ can be split into two parts:

$$\frac{p_v(T_\infty)-p}{\rho_l}=\frac{p_v-p}{\rho_l}+\frac{p_v(T_\infty)-p_v}{\rho_l} \tag{56}$$

where p_v is the vapour pressure based on local liquid temperature. $p_v(T_\infty)-p_v$ is the vapour pressure depression owing to liquid temperature difference $T_\infty-T_v$. As the first-order approximation, there is a relationship between the two depressions:

$$\frac{p_v(T_\infty)-p_v}{\rho_l}=\frac{1}{\rho_l}\frac{dp_v}{dT_l}(T_\infty-T_v) \tag{57}$$

where $T_\infty - T_v$ is liquid temperature depression. The depression is calculated with the B-factor-based formula [198]

$$T_\infty - T_v = B\frac{\rho_v L}{\rho_l C_{pl}}, B=\frac{\alpha_v}{1-\alpha_v} \tag{58}$$

where L is liquid latent heat, c_{pl} is liquid specific heat.

Putting Eqs.(57)-(58) into Eq.(56), and $p_v(T_\infty) - p$ is expressed with local transmural pressure $p_v - p$ and temperature depression explicitly

$$\frac{p_v(T_\infty)-p}{\rho_l}=\frac{p_v-p}{\rho_l}+\frac{1}{\rho_l}\frac{dp_v}{dT_l}\frac{\alpha_v}{1-\alpha_v}\frac{\rho_v L}{\rho_l C_{pl}} \tag{59}$$

and the simplified Rayleigh-Plesset equation is rewritten as

$$\frac{3}{2}\left(\frac{dR}{dt}\right)^2+\frac{4\nu}{R}\frac{dR}{dt}=\frac{p_v-p}{\rho_l}+\frac{1}{\rho_l}\frac{dp_v}{dT_l}\frac{\alpha_v}{1-\alpha_v}\frac{\rho_v L}{\rho_l C_{pl}} \tag{60}$$

Likewise, the vapour bubble growth rate is expressed by

$$\frac{dR}{dt}=\frac{1}{3}\left[\sqrt{6\left(\frac{p_v-p}{\rho_l}+\frac{1}{\rho_l}\frac{dp_v}{dT_l}\frac{\alpha_v}{1-\alpha_v}\frac{\rho_v L}{\rho_l C_{pl}}\right)+\left(\frac{4\nu}{R}\right)^2}-\frac{4\nu}{R}\right] \tag{61}$$

As a result, the ZGB cavitation model Eq. (34) is modified as the following after setting R=R_0

$$\dot{m}=\begin{cases} F_{vap}\dfrac{\alpha_{nc}(1-\alpha_v)\rho_v}{R_0}\left[\sqrt{6\left(\dfrac{p_v-p}{\rho_l}+\dfrac{1}{\rho_l}\dfrac{dp_v}{dT_l}\dfrac{\alpha_v}{1-\alpha_v}\dfrac{\rho_v L}{\rho_l C_{pl}}\right)+\left(\dfrac{4\nu}{R_0}\right)^2}-\dfrac{4\nu}{R_0}\right], & \text{if} p\le p_v \\ F_{con}\dfrac{\alpha_v\rho_v}{R_0}\left[\sqrt{6\left(\dfrac{p-p_v}{\rho_l}+\dfrac{1}{\rho_l}\dfrac{dp_v}{dT_l}\dfrac{\alpha_v}{1-\alpha_v}\dfrac{\rho_v L}{\rho_l C_{pl}}\right)+\left(\dfrac{4\nu}{R_0}\right)^2}-\dfrac{4\nu}{R_0}\right], & \text{else} \end{cases} \tag{62}$$

Eq.(62) is the cavitation model proposed by [203]. Unfortunately, the model fails to handle the thermodynamic effect at all, although the local transmural pressure and temperature depression are included. It is incorrect because a constant $p_v(T_\infty)$ is used in Eq.(55). Although the temperature-dependent p_v and temperature depression are included, they cancel each other out. Using Eq.(59), the cavitation model Eq.(62) should be in the following form:

$$\dot{m}=\begin{cases} F_{vap}\dfrac{\alpha_{nc}(1-\alpha_v)\rho_v}{R_0}\left\{\sqrt{6\left[\dfrac{p_v(T_\infty)-p}{\rho_l}-\dfrac{1}{\rho_l}\dfrac{dp_v}{dT_l}\dfrac{\alpha_v}{1-\alpha_v}\dfrac{\rho_v L}{\rho_l C_{pl}}\right]+\left(\dfrac{4\nu}{R_0}\right)^2}-\dfrac{4\nu}{R_0}\right\}, & \text{if } p\le p_v \\ F_{con}\dfrac{\alpha_v\rho_v}{R_0}\left\{\sqrt{6\left[\dfrac{p-p_v(T_\infty)}{\rho_l}-\dfrac{1}{\rho_l}\dfrac{dp_v}{dT_l}\dfrac{\alpha_v}{1-\alpha_v}\dfrac{\rho_v L}{\rho_l C_{pl}}\right]+\left(\dfrac{4\nu}{R_0}\right)^2}-\dfrac{4\nu}{R_0}\right\}, & \text{else} \end{cases} \tag{67}$$

$$\dot{m}=\begin{cases} F_{vap}\dfrac{\alpha_{nc}(1-\alpha_v)\rho_v}{R_0}\left[\sqrt{6\dfrac{p_v(T_\infty)-p}{\rho_l}+\left(\dfrac{4\nu}{R_0}\right)^2}-\dfrac{4\nu}{R_0}\right], & \text{if } p\le p_v \\ F_{con}\dfrac{\alpha_v\rho_v}{R_0}\left[\sqrt{6\dfrac{p-p_v(T_\infty)}{\rho_l}+\left(\dfrac{4\nu}{R_0}\right)^2}-\dfrac{4\nu}{R_0}\right], & \text{else} \end{cases} \tag{63}$$

Obviously, Eq.(63) contains nothing about the thermodynamic effect in cavitation, although it has included the liquid viscosity.

The right way of allowing a cavitation model to have temperature depression is to adopt the simplified Rayleigh-Plesset equation Eq.(52) as the fundamental equation. The pressure depression term will occur by adding and subtracting $p_v(T_\infty)$, namely

$$\frac{3}{2}\left(\frac{dR}{dt}\right)^2+\frac{4\nu}{R}\frac{dR}{dt}=\frac{p_v(T_\infty)-p}{\rho_l}-\frac{p_v(T_\infty)-p_v}{\rho_l} \tag{64}$$

After Eqs.(57) and (58) being considered, the simplified Rayleigh-Plesset equation is recast as

$$\frac{3}{2}\left(\frac{dR}{dt}\right)^2+\frac{4\nu}{R}\frac{dR}{dt}=\frac{p_v(T_\infty)-p}{\rho_l}-\frac{1}{\rho_l}\frac{dp_v}{dT_l}\frac{\alpha_v}{1-\alpha_v}\frac{\rho_v L}{\rho_l C_{pl}} \tag{65}$$

The corresponding vapour bubble growth rate and cavitation model are derived as

$$\frac{dR}{dt}=\frac{1}{3}\left[\sqrt{6\left[\frac{p_v(T_\infty)-p}{\rho_l}-\frac{1}{\rho_l}\frac{dp_v}{dT_l}\frac{\alpha_v}{1-\alpha_v}\frac{\rho_v L}{\rho_l C_{pl}}\right]+\left(\frac{4\nu}{R}\right)^2}-\frac{4\nu}{R}\right] \tag{66}$$

and

In fact, the model Eq.(67) is essentially identical to the model Eq. (54), but inferior to the latter, since dp_v/dT_l cannot be estimated accurately, and $\alpha_v/(1-\alpha_v)\to\infty$, if $\alpha_v\to 1$.

3.4. Other cavitation models and issues

3.4.1. Rankine vortex cavitation model

Simulations of unsteady cavitating flow over a hydrofoil can be challenging because the cavity is subject to a periodic process including formation, breakup, shedding and collapse [204]. To address this challenging, a Rankine vortex cavitation model was initiated in [205]. In the model, a cavity is assumed to be trapped in a Rankine vortex in a viscous fluid and the spherical cavity size is identical to the central core size of the vortex. The cavity is carried downstream by the moving vortex and experiences a formation-breakup-shedding-collapse cycle. The pressure profile in a cavitating Rankine vortex p_{vortex} is expressed by

$$p_{vortex} = \begin{cases} p_v, \ \text{incentralcore} \ (r \le R_{core}) \\ p - \dfrac{\rho_l \Gamma^2}{8\pi^2} \dfrac{1}{r^2}, \ \text{outsidethecore} \ (r \ge R_{core}) \end{cases} \tag{68}$$

where R_{core} is the central core radius, p is the pressure outside the vortex, while Γ is vortex circulation depending on the rotating function of a flow in terms of the Galilean-invariant, which is the ratio of the shear rate to the vorticity magnitude. The core size has been decided by Eq.(68) with the condition $p_v = p - \frac{\rho_l \Gamma^2}{8\pi^2} \frac{1}{R_{core}^2}$ and is demonstrated by

$$R_{core} = \frac{\Gamma}{2\pi} \sqrt{\frac{1}{2} \frac{\rho_l}{p - p_v}} \tag{69}$$

Based on Eq.(18) the vapour bubble growth rate as a function of R_{core} can be determined. Based on Eq.(37), with an approximation $\rho_l \approx \rho$, the corresponding mass transfer rate can be calculated by

$$\dot{m} = \frac{3\alpha_v \rho_v}{R_{core}} \sqrt{\frac{2}{3} \frac{p - p_v}{\rho_l}} = 2\sqrt{3} \left(\frac{2\pi}{\Gamma}\right) \frac{\alpha_v \rho_v (p - p_v)}{\rho_l} \tag{70}$$

Like Eq.(39), the cavitation model based on Eq. (70) is written as

$$\dot{m} = \begin{cases} F_{vap} \left(\dfrac{2\pi}{\Gamma}\right) \dfrac{(1 - \alpha_v)\rho_v (p_v - p)}{\rho_l}, \ \text{if} \ p \le p_v \\ F_{con} \left(\dfrac{2\pi}{\Gamma}\right) \dfrac{\alpha_v \rho_v (p - p_v)}{\rho_l}, \ \text{else} \end{cases} \tag{71}$$

where F_{vap} and F_{con} are calibrated coefficients for evaporation and condensation, respectively; $2\pi/\Gamma$ is the rotating function depending on local shear rate and vorticity, and a curve of the function can be found in [205]. Compared with the cavity cycle predicted using the ZGB model, this model exhibits an ability to capture vapour bubble breakup process. Furthermore, the power spectrum curve predicted is close to the experiment. Compared with Eq.(9), Eq.(71) seems to provide physical evidence for the arbitrary mass transfer rate model.

3.4.2. Bubble-bubble interaction

In the cavitation models above, even though nucleation theories of vapour bubbles are taken into account in the cavitation inception stage, the interaction of bubbles in a vapour bubble cloud/cluster has not been considered. The interaction between bubbles is important in the bubble collapse period and it has been studied experimentally and analytically since the 1980's [129]. Initially, the case where there are two vapour bubbles in a fixed position was studied. In this case, there are Bjerknes forces due to the superposition of the potential functions induced by neighbouring bubbles. Then, the Bjerknes forces between small cavitation bubbles are taken into account in the Rayleigh-Plesset equation. Finally, the equation was solved numerically to decide bubble radius and internal pressure in response to liquid transient pressure. Some typical studies of this nature can be found in [206–208]. In parallel, a few studies [209,210] were devoted to considering the case with more than two bubbles, i.e., a cloud/cluster of bubbles, by using the perturbation method in the Rayleigh-Plesset equation. Although a two-phase flow model for a cloud of vapour bubbles was proposed in 1984 [211], it has found few applications to analyse the interaction between vapour bubbles so far [212].

Recently, the Rayleigh-Plesset equation for two vapour bubbles with fixed position in [207,208] was employed to develop a new cavitation model for CFD with the interaction between bubbles [213]. The phase change rates deduced are slightly more complex than Eq.(37), which has five empirical constants or correlations. The experimental nuclei number density was included in the model. When the model was used to predict the head-NPSH (net positive suction head) curve of an experimental centrifugal pump, it failed to demonstrate a better accuracy against the observations than the ZGB cavitation model in ANSYS CFX does [214]. Nevertheless, more validation work on the model is needed in future.

In [215], a theoretical model of gas bubble breakup in a liquid isotropic turbulent flow was proposed. The evolution of the probability distribution density of bubble radius was determined using turbulence energy distribution over different length scales. The situation of vapour bubble breakup downstream cavity was considered as the same as that of gas bubble breakup in a turbulence flow [216], while the number of vapour bubbles in collapse was estimated with the model of [215]. The mass transfer rate in the full cavitation model in condensation was then replaced with a new formula where the bubble radius was expressed by the number of bubbles and vapour volume fraction, but the mass transfer rate in evaporation remains unchanged [215]. LES of cavitating flow was conducted on a cubic bubble cloud with lattice bubble distribution arranged and a semi-empirical formula for the condensation process was developed [217] to improve computational accuracy. The collapse pressure predicted with this model is slightly higher than the full cavitation model. Note that the bubble–bubble interaction doesn't seem to be considered explicitly.

Recently, a mutual interaction model between two spherical vapour bubbles in different sizes was derived. Two vapour bubbles are fixed in their positions in water, and the water in the far-field is stationary, while the water near the bubbles is in potential flow induced by the radius growth or collapse of two bubbles. The mass and momentum conservation equations, coupled with the local flow divergence, were solved to obtain the evolution of the bubble radii and local pressure. However, the model shows that the bubble–bubble interaction plays a primary role in cavitation inception [218]. Therefore, it remains unclear whether the bubble–bubble interaction should be taken into account in cavitation models.

3.4.3. Cavitation models with first principal stress

Cavitation is similar to fracture in solid materials. It can take place in liquid if the tensile stress in one direction is beyond a threshold. Thus, the cavitation threshold in a flowing liquid should be the maximum tensile stress that the fluid can sustain. In this context, the cavitation criterion is expressed as [219]

$$\sigma_{11} \ge -p_v \tag{72}$$

where σ_{11} is the first principal stress in a flow field. For 3D turbulent flows, the first principal stress σ_{11} is expressed by [220]

$$\sigma_{11} = -p + (\mu + \mu_t)\sqrt{2S_{ij}S_{ij}} \quad \text{and} \quad S_{ij} = \frac{1}{2}\left(\frac{\partial u_i}{\partial x_j} + \frac{\partial u_j}{\partial x_i}\right) \tag{73}$$

where μ is liquid dynamic viscosity, μ_t is turbulent eddy viscosity, S_{ij} are time-averaged velocity deformation rate tensor, u_i and u_j are time-averaged velocity components in the Cartesian coordinate system along the i and j coordinate directions, respectively, $i,j = 1,2,3$.

Ignoring turbulence contribution to the threshold, the cavitation criterion in terms of the first principal stress for 3D turbulent flows is expressed as

$$-p + (\mu + \mu_t)\sqrt{2S_{ij}S_{ij}} \ge -p_v \tag{74}$$

Eq.(74) was combined with the Schnerr-Sauer cavitation model Eq. (21) to establish a cavitation model. The model was then implemented in OpenFOAM to compute cavitating flows over a 3D hydrofoil [220].

For 2D turbulent flows, the first principal stress σ_{11} is simplified as [221]

$$\sigma_{11} = -p + (\mu + \mu_t) S_{max} \tag{75}$$

where S_{max} is the maximum shear rate.

Likewise, when the turbulence effect on the pressure threshold is taken into account, the cavitation criterion in terms of the first principal stress is written as [221]

$$(p_v + p_t) + (\mu + \mu_t) S_{max} - p \geq 0 \tag{76}$$

where $p_t = 0.47\rho k$,ρ is mixture density, k is turbulent kinetic energy.

Based on Eq.(76), the cavitation model with the first principal stress was proposed in [221] on basis of the Schnerr-Sauer cavitation model [90]. The corresponding mass transfer rates read as\

$$\dot{m} = \begin{cases} \dfrac{3(\alpha_v + \alpha_g)\rho_l \rho_v}{R_0[\rho + \alpha_g(\rho_l - \rho_g)]} \sqrt{\dfrac{2[p_v + p_t + (\mu + \mu_t)\dot{s}_{max} - p]}{3\rho_l}}, & \text{if } p \leq p_v + p_t + (\mu + \mu_t) S_{max} \\ -\dfrac{3(\alpha_v + \alpha_g)\rho_l \rho_v}{R_0[\rho + \alpha_g(\rho_l - \rho_g)]} \sqrt{\dfrac{2[p - p_v - p_t - (\mu + \mu_t)\dot{s}_{max}]}{3\rho_l}}, & \text{else} \end{cases} \tag{77}$$

where ρ_g is non-condensable gas density in a liquid. The model has been applied to simulate unsteady turbulent cavitating flows of water around a 2D Clark-Y hydrofoil. The better lift and drag coefficients were obtained against the experimental data in comparison with the ZGB cavitation model.

3.4.4. Stochastic-field cavitation model

Essentially, cavitation is a stochastic process from nuclei size, inception, development to collapse. These elementary processes can be described with probability density functions (PDF) and their transport models. In [222], a stochastic-field cavitation model was developed based on the Rayleigh-Plesset equation and a PDF of bubble size for the stochastic field method in [223]. The model was validated with the experimental cavitating flows in venturi and fluidic diode.

3.4.5. Methods for model constant calibration

In the cavitation models summarised above, there are two constants for evaporation and condensation. These empirical constants need to be calibrated against experimental data of cavitating flow prior to a specific application. It is noted that the model constants in the full cavitation model, ZGB and Kunz models were optimized based on the pressure coefficient profile of cavitating flow over NACA66 (6° incidence, 1.08, 1.25, 1.48 and 1.79 cavitation numbers, 2×10^6 Reynolds number) and NACA009 (2.5° incidence, 0.75, 0.81 and 0.90 cavitation numbers, 2×10^6 Reynolds number) in water tunnels [224]. ANSYS CFX is used to obtain a pressure coefficient profile, and the profile was read into optimizer-modeFRONTIER to decide the model constants. This procedure is repeated until the predicted profile in agreement with the experimental one in an allowable small error. The multi-objective genetic optimization algorithm (MOGA-II) was employed in search for the optimum solution.

An even more general method for optimizing the model constants in the ZGB cavitation model was designed in [225]. Firstly, sampling points of two model constants were generated by using optimal Latin hypercube design in a domain, and the pressure coefficient profiles of the cavitating flows over the hydrofoil NACA66 in a wide range of flow conditions (incidence and cavitation number) were obtained by using OpenFOAM. Secondly, a surrogate model was built so the optimum model constants were determined by means of the sequential approximate optimization (SAO) method for each of flow conditions. Finally, the optimum model constants for a specific flow condition can be interpolated from those optimized model constants array by making use of the radial basis function neural network (RBFNN) in MATLAB. A very similar work on optimization of the model constants in the Kunz cavitation model was reported in [226] against experimental data on a hydrofoil and hemispherical head-form. A machine learning method has been employed to optimize the model constants in the Kunz cavitation model against the experimental cavity size in a propeller [227].

4. Discussion

The working fluids in ORC systems have a more notiably thermo-sensitive property in cavitation due to their lower boiling temperature compared with water. Hence, these fluids require a higher suction pressure and a smaller NPSH than water. A higher suction pressure adds the cost of equipment, while the smaller NPSH can reduce the elevation level of the fluid container installation, reducing costs. Since the vapour pressure of these working fluids decreases with temperature, subcooling the liquid working fluid before entering a feed pump can be used to suppress cavitation within the pump. Nonetheless, the subcooling may be cost-effective. To reduce the cost of the working fluid feeding system in ORC systems, some cavitation may be allowable in the feed pump. However, the cavitation might result in instabilities of fluid flow exiting the feed pump, ultimately induce oscillations in the system operation. Therefore, cavitating flows of working fluids in ORC systems need to be investigated extensively.

CFD simulations are one of the most promising methods for dealing with cavitating flows of working fluids in ORC systems. Unfortunately, this sort of CFD simulations has little been seen in the literature so far. Firstly, the existing CFD packages such as ANSYS CFX or Fluent or STAR-CCM + or OpenFOAM or even CATUM can be used to model cavitating flows, provided that the constants in their cavitation models have been calibrated with available experimental data of similar organic fluids in advance.

Secondly, we can develop our own cavitating models with thermodynamic effect. In fact, a number of cavitation models with the effect have emerged, the cavitation regime shown in Fig. 5, however, has not been considered and implemented properly. Potentially, Eq.(51) can be employed to determine vapour bubble growth rate for cavitation models in various cavitation regimes. For this purpose, the article [228] has provided an excellent review.

Thirdly, as mentioned in Section 2.1, the interface tracking model has a difficulty in treating 3D cavitating flows. Recently, a VOF method combined with pool boiling and cavitation inception models was developed to track 3D interface between liquid and vapour [229]. The VOF method for pool boiling problem is originated from [230] and [231], and the cavitation inception model is descripted in [105]. The cavitating flow of the mixture of liquid and vapour is unsteady, compressible and laminar and described by using the Reynolds-averaged

Navier-Stokes equations. This approach likely can be applied to cavitating flows with thermal effect in future.

Fourthly, an extension to the classical homogeneous nucleation theory in Section 2.2.5 was presented in [232] to explain the discrepancy between theoretical prediction and experimental observation of nucleation rates in water at normal temperature. The thermodynamic fluctuation theory was used to derive the model for the formation of bubble nucleus. The non-equilibrium effects in nuclei formation were considered with correction coefficients determined experimentally. This framework may be useful to build the thermodynamic model for nucleation rate in organic fluids in future.

Working fluids in ORC systems may be operated in subcooled conditions to avoid cavitation in feed pumps. The subcooling degree needs to be determined numerically or experimentally. The vapour bubble growth and collapse have been investigated analytically in [186]. Currently, cavitation models in subcooled liquids are unavailable. Recently, vapour bubble growth during subcooled nucleate boiling on a vertical heater was tested and it turned out that existing bubble growth models cannot account for the heater surface characteristics extensively [233,234], which suggests that developing a cavitation model for subcooled liquids is challenging and more efforts are needed.

Nucleation cavitation models for organic fluids in ORC systems should be based on non-condensable gas and solid particles nuclei. The non-condensable gas concentration should also be included in the models, too. For example, at total pressure (air plus vapour) 1 atm, air-saturated R114 contains about 140 ppm (mg/kg liquid) non-condensable gas at 0℃, and about 1000 ppm at –32℃ [235]. For comparison, the non-condensable gas concentration is 22 ppm in water at 25℃ and 1 atm.

The non-condensable gas in a liquid can play an important role in a cavitating flow. Firstly, the gas shares the same velocity with the liquid, and the gas mass flow rate remains unchanged in the flow field, but the gas pressure, volume or temperature may vary in ideal gas law (isothermal process) or polytropic law (adiabatic process), depending on specific situations. Secondly, the non-condensable gas serves as cavitation nucleation sites. Nonetheless, the gas partial pressure raises the pressure threshold for cavitation inception. To properly consider the effect of non-condensable gas on cavitation, we must propose a process law for such a gas, and include its volume fraction in the mixture density and reflect the gas partial pressure in the Rayleigh-Plesset equation Eq. (17). When the non-condensable gas is assumed to be in spherical bubbles, a general process law has been proposed for the gas in [90], which is described by

$$p_g = p_{g0}\left(\frac{R_{g0}}{R_g}\right)^{3\varkappa} \tag{78}$$

where p_{g0} and R_{g0} are initial partial pressure and bubble radius of the non-condensable gas in a liquid, respectively; $\varkappa$ is polytropic index, $\varkappa$=1 for isothermal cavitation (isothermal process),$\varkappa = c_{pg}/c_{vg}$for cavitation with thermodynamic effect (adiabatic process), c_{pg} and c_{vg} are specific heat capacities of the gas at constant pressure and constant volume, respectively.

In [85,103,111,236–238], the non-condensable gas was taken into account in the mixture density and liquid phase volume fraction only. In [145,239,240], however, the gas was presented in the Rayleigh-Plesset equation alone in terms of partial pressure. The effect of non-condensable gas is not included in the mixture density, the liquid phase volume fraction, and the threshold for cavitation inception in terms of partial pressure in the literature at the same time. If the non-condensable gas is adopted in the mixture density and liquid phase volume fraction, the gas will appear in the liquid prior to the vapour with decreasing suction pressure in a centrifugal pump, exhibiting pseudo-cavitation phenomenon [241]. The pseudo-cavitation effect of nitrogen (non-condensable gas) in fuel through diesel injector nozzles was simulated by using three-components (nitrogen, liquid isooctane plus vapour isooctane) mixture model and the Schnerr-Sauer cavitation model [242]. It was demonstrated that as the pressure stabilizes at a pressure higher than the saturation pressure, the pseudo-cavitation effect takes over vapour cavitation. In a reciprocating pump, the non-condensable gas occurs on the plunger surface at first in suction stroke [243]. Obviously, these studies have laid a solidary basis for considering non-condensable gas in cavitating flow simulations of organic fluids.

Diaphragm reciprocating pumps are commonly applied to circulate the organic fluid in ORC systems. The transient cavitating flow can appear through the gap between the moving suction valve and the valve seat in the pump liquid end, as shown in Fig. 2. The flow can involve vortex formation, breakup and shedding processes to carry vapour cavities downstream. To better capture large to medium-small-scale flow structures in these processes, LES presented in [244–249] is worth being attempted in computation of the cavitating flow in a diaphragm pump in future.

5. Conclusions

A systematic review of cavitation models with thermodynamic effect potentially applied to CFD simulations of cavitating flows in feed pumps in organic Rankine cycle systems has been presented. The existing cavitation models are classified and listed methodically and comprehensively. The characteristics of those cavitation models are identified and critically analysed in terms of mathematical formula, fluid mechanics, or heat transfer. Methods for implementing thermodynamic effect in cavitation models are clarified and demonstrated. Additionally, a few newly developed cavitation models such as cavitation models with liquid viscosity, Rankine vortex cavitation model, cavitation models with bubble–bubble interaction, and cavitation models with bubble breakup in the cavity cloud are explained. Discussion about and the prospect of cavitation models are provided. Compared with fully coupled multiscale cavitation models, homogeneous mixture cavitation models require much less computational resources, and the thermodynamic effect can be easily implemented in them. Although the thermodynamic effect has been implemented in the existing cavitation models, the cavitation regimes, namely inertia-controlled, heat-diffusion controlled and intermediate states in between, have not been applied in a proper way. Nucleation cavitation models for organic fluids in organic Rankine cycle power plants should be proposed based on the measured nuclei and non-condensable gas concentration in organic fluids.

Declaration of Competing Interest

The authors declare that they have no known competing financial interests or personal relationships that could have appeared to influence the work reported in this paper.

Acknowledgements

The work was supported financially by EPSRC in the UK (EP/N020472/1, EP/N005228/1, EP/P028829/1, EP/R003122/1 and EP/T022701/1). Also, special thanks were owed to Dr Hongyang Li who spent time on English correction and Mr Michael-Allan Millar who corrected English text and offered constructive suggestions to improve the presentation of the content in the article.

References

[1] H.J. Chen, D.Y. Goswami, E.K. Stefanakos, A review of thermodynamic cycles and working fluids for the conversion of low-grade heat, Renew. Sustain. Energy Rev. 14 (2010) 3059–3067.
[2] S. Quoilin, M. VanDenBroek, S. Declaye, Techno-economic survey of organic Rankine cycle (ORC) systems, Renew. Sustain. Energy Rev. 22 (2013) 168–186.
[3] B.F. Tchanche, M. Pétrissans, G. Papadakisc, Heat resources and organic Rankine cycle machines, Renew. Sustain. Energy Rev. 39 (2014) 1185–1199.

[4] P. Colonna, E. Casati, C. Trapp, et al., Organic Rankine cycle power systems: from the concept to current technology, applications, and an outlook to the future, ASME J. Eng. Gas Turbines Power 137 (10) (2015).
[5] B.S. Park, M. Usman, Imran, et al, Review of organic Rankine cycle experimental data trends, Energy Convers. Manage. 173 (2018) 679–691.
[6] N. Yamada, M. Watanabe, A. Hoshi, et al., Experiment on pumpless Rankine-type cycle with scroll expander, Energy 49 (2013) 137–145.
[7] P. Gao, L.W. Wang, R.Z. Wang, et al., Experimental investigation on a small pumpless ORC (organic Rankine cycle) system driven by the low temperature heat source, Energy 91 (2015) 324–333.
[8] E.S. Richardson, Thermodynamic performance of new thermofluidic feed pumps for Organic Rankine Cycle applications, Appl. Energy 161 (2016) 75–84.
[9] G. Shu, Z. Yu, P. Liu, et al., Potential of a thermofluidic feed pump on performance improvement of the dual-loop Rankine cycle using for engine waste heat recovery, Energy Convers. Manage. 171 (2018) 1150–1162.
[10] M. Usman, Imran, Park B S, et al, Multi-objective optimization of evaporator of organic Rankine cycle (ORC) for low temperature geothermal heat source, Appl. Therm. Eng. 80 (2015) 1–9.
[11] K. Rahbar, S. Mahmoud, R.K. Al-Dadah, et al., Modelling and optimization of organic Rankine cycle based on a small-scale radial inflow turbine, Energy Convers. Manage. 91 (2015) 186–198.
[12] A. Borsukiewicz-Gozdur, Pumping work in the organic Rankine cycle, Appl. Therm. Eng. 51 (2013) 781–786.
[13] A. Landelle, N. Tauveron, P. Haberschill, et al., Organic Rankine cycle design and performance comparison based on experimental database, Appl. Energy 204 (2017) 1172–1187.
[14] Y.X. Yang, H.G. Zhang, Y.H. Xu, et al., Matching and operating characteristics of working fluid pumps with organic Rankine cycle system, Appl. Therm. Eng. 142 (2018) 622–631.
[15] Y.X. Yang, H.G. Zhang, G.H. Tian, et al., Performance analysis of a multistage centrifugal pump used in an organic Rankine cycle (ORC) system under various condensation conditions, J. Therm. Sci. 28 (4) (2019) 621–634.
[16] X. Wang, Y.Q. Feng, T.C. Hung, Investigating the system behaviors of a 10kW organic Rankine cycle (ORC) prototype using plunger pump and centrifugal pump, Energies 13 (5) (2020) 1141.
[17] T.Z. Kaczmarczyk, G. Żywica, E. Ihnatowicz, Experimental investigation on a rotodynamic pump operating in the cogeneration system with a low-boiling working medium, Trans. Inst. Fluid-Flow Machinery 134 (2016) 63–87.
[18] E. Bollina, Head-flow and npsh performance of an axial piston pump working with organic fluids at different temperatures, Int. J. Heat Fluid Flow 5 (2) (1984) 93–100.
[19] E.J. Bala, P.W. O'Callaghan, S.D. Probert, Influence of organic working fluids on the performance of a positive-displacement pump with sliding vanes, Appl. Energy 20 (1985) 153–159.
[20] G. Bianchi, F. Fatigati, S. Murgia, et al., Modeling and experimental activities on a small-scale sliding vane pump for ORC-based waste heat recovery applications, Energy Procedia 101 (2016) 1240–1247.
[21] J.C. Chang, T.C. Hung, Y.L. He, et al., Experimental study on low-temperature organic Rankine cycle utilizing scroll type expander, Appl. Energy 155 (2015) 150–159.
[22] X.F. Yang, J.L. Xu, Z. Miao, et al., Operation of an organic Rankine cycle dependent on pumping flow rates and expander torques, Energy 90 (2015) 864–878.
[23] Landelle A, Tauveron N, Haberschill P, et al, Study of reciprocating pump for supercritical ORC at full and part load operation, Proceedings of the 3rd International Seminar on ORC Power Systems (ASME ORC 2015), 12-14 October, 2015, Brussels, Belgium.
[24] A. Landelle, N. Tauveron, R. Revellin, et al., Performance investigation of reciprocating pump running with organic fluid for organic Rankine cycle, Appl. Therm. Eng. 113 (2017) 962–969.
[25] G. Carrato, P. Pallis, A.D. Leontaritis, et al., Experimental performance evaluation of a multi-diaphragm pump of a micro-ORC system, Energy Procedia 129 (2017) 1018–1025.
[26] F. D'Amico, P. Pallis, A.D. Leontaritis, et al., Semi-empirical model of a multi-diaphragm pump in an Organic Rankine Cycle (ORC) experimental unit, Energy 143 (2018) 1056–1071.
[27] N. Casari, E. Fadiga, M. Pinelli, et al., Pressure pulsation and cavitation phenomena in a micro-ORC system, Energies 12 (2019) 2186.
[28] C. Brennen, The dynamic behaviour and compliance of a stream of cavitating bubbles, ASME J. Fluids Eng. 95 (4) (1973) 533–541.
[29] W. Li, Z. Yu, Correction of cavitation with thermodynamic effect for a diaphragm pump in organic Rankine cycle systems, Energy Rep. 6 (3) (2020) 2956–2972.
[30] M.L. Zhang, R.Q. Liao, J. Feng, Hydrokinetic numerical simulation for sucking performance of reciprocating pump, Trans. Chin. Soc. Agric. Eng. 26 (Supp. 2) (2010) 242–247.
[31] A. Iannetti, M. Stickland, W.M. Dempster, A computational fluid dynamics model to evaluate the inlet stroke performance of a positive displacement reciprocating plunger pump, Proc. Mech. Part A: J. Power Energy 228 (5) (2014) 574–584.
[32] A. Iannetti, M.T. Stickland, W.M. Dempster, A CFD study on the mechanisms which cause cavitation in positive displacement reciprocating pumps, J. Hydraul. Eng. 1 (2015) 47–59.
[33] A. Iannetti, M. Stickland, W.M. Dempster, A CFD and experimental study cavitation in positive displacement pumps: Benefits and drawbacks of the full cavitation model, Eng. Applications Comput. Fluid Mech. 10 (1) (2016) 57–71.
[34] L.F. Ma, J. Feng, Y. Liu, et al., Numerical simulation of optimization of head loss and cavitation for reciprocating pump, Chin. Hydraul. Pneumatics 3 (2019) 132–137.
[35] G. Zhu, S.M. Dong, Analysis on the performance improvement of reciprocating pump with variable stiffness valve using CFD, J. Appl. Fluid Mech. 13 (2) (2020) 387–400.
[36] W. Li, Z. Yu, Cavitating flows of organic fluid with thermodynamic effect in a diaphragm pump for organic Rankine cycle systems, Energy 237 (10) (2021) 121495.
[37] Y. Utturkar, J. Wu, G. Wang, et al., Recent progress in modeling of cryogenic cavitation for liquid rocket propulsion, Prog. Aerosp. Sci. 41 (2005) 558–608.
[38] C.C. Tseng, Y. Wei, G. Wang, et al., Modeling of turbulent, isothermal and cryogenic cavitation under attached conditions, Acta Mech. Sin. 26 (3) (2010) 325–353.
[39] A. Niedzwiedzka, G.H. Schnerr, W. Sobieski, Review of numerical models of cavitating flows with the use of the homogeneous approach, Arch. Thermodyn. 37 (2) (2016) 71–88.
[40] X.W. Luo, B. Ji, Y. Tsujimoto, A review of cavitation in hydraulic machinery, J. Hydrodyn. 28 (3) (2016) 335–358.
[41] G. Wang, Q. Wu, B. Huang, Dynamics of cavitation-structure interaction, Acta Mech. Sin. 33 (4) (2017) 685–708.
[42] H. Nishikawa, Y. Matsumoto, H. Ohashi, Numerical calculation of the bubble two-phase flow around an airfoil, Comput. Fluids 19 (3/4) (1991) 453–460.
[43] C. Brennen, A numerical solution of axisymmetric cavity flows, J. Fluid Mech. 37 (4) (1969) 671–688.
[44] H. Lemonnier, A. Rowe, Another approach in modelling cavitating flows, J. Fluid Mech. 195 (1988) 557–580.
[45] C. Pellone, A. Rowe, Effect of separation on partial cavitation, ASME J. Fluid Eng. 110 (2) (1988) 182–189.
[46] M. Deshpande, J. Feng, C.L. Merkle, Cavity flow predictions based on the Euler equations, ASME J. Fluids Eng. 116 (1) (1994) 36–44.
[47] L. Liu, J. Li, Z. Feng, A numerical method for simulation of attached cavitation flows, Int. J. Numer. Meth. Fluids 52 (2006) 639–658.
[48] M. Deshpande, J. Feng, C.L. Merkle, Numerical modelling of the thermodynamic effects of cavitation, ASME J. Fluids Eng. 119 (2) (1997) 420–426.
[49] T. Tokumasu, Y. Sekino, K. Kamijo, The numerical analysis of the effect of flow properties on the thermodynamic effect of cavitation, Trans. Japan Soc. Aeronaut. Space Sci. 156 (47) (2004) 146–152.
[50] P. Cooper, Analysis of single- and two-phase flows in turbopump inducers, ASME J. Eng. Power 89 (4) (1967) 577–586.
[51] Y. Ventikos, A. Tzabiras, numerical method for the simulation of steady and unsteady cavitating flows, Comput. Fluids 29 (2000) 63–88.
[52] G.H. Schnerr, I.H. Sezal, S.J. Schmidt, Numerical investigation of three-dimensional cloud cavitation with special emphasis on collapse induced shock dynamics, Phys. Fluids 20 (2008) 040703.
[53] Y. Chen, S.D. Heister, Two-phase modelling of cavitating flows, Comput. Fluids 24 (7) (1995) 799–809.
[54] K. Okita, T. Kajishima, Numerical simulation of unsteady cavitating flows around a hydrofoil, Trans. JSME-Ser. B 68 (667) (2002) 637–644.
[55] Y. Delannoy, J.L. Kueny, Two phase flow approach in unsteady cavitation modelling, Cavitation Multiphase Flow Forum, ASME-FED 98 (1990) 153–158.
[56] O. Coutier-Delgosha, J.L. Reboud, Y. Delannoy, Numerical simulation of the unsteady behaviour of cavitating flows, Int. J. Numer. Meth. Fluids 42 (2003) 527–554.
[57] J.L. Reboud, O. Coutier-Delgosha, B. Pouffary, et al., Numerical simulation of unsteady cavitating flows: some applications and open problems 1–4 (November 2003) 1–10.
[58] E. Goncalves, R.F. Patella, J. Rolland, et al., Thermodynamic effect on a cavitating inducer in liquid hydrogen, ASME J. Fluids Eng. 132 (11) (2010) 111305.
[59] E. Goncalves, R.F. Patella, Numerical simulation of cavitating flows with homogeneous models, Comput. Fluids 38 (2009) 1682–1696.
[60] J. Decaix, E. Goncalves, Investigation of three-dimensional effects on a cavitating Venturi flow, Int. J. Heat Fluid Flow 44 (2013) 576–595.
[61] E. Goncalves, R.F. Patella, Constraints on equation of state for cavitating flows with thermodynamic effects, Appl. Math. Comput. 217 (2011) 5095–5102.
[62] E. Goncalves, Numerical study of expansion tube problems: Toward the simulation of cavitation, Comput. Fluids 72 (2013) 1–19.
[63] E. Goncalves, Modeling for non isothermal cavitation using 4-equation models, Int. J. Heat Mass Transf. 76 (2014) 247–262.
[64] E. Goncalves, B. Charriere, Modelling for isothermal cavitation with a four-equation model, Int. J. Multiph. Flow 59 (2014) 54–72.
[65] E. Goncalves, D. Zeidan, Numerical study of turbulent cavitating flows in thermal regime, Int. J. Numer. Meth. Heat Fluid Flow 27 (7) (2017) 1487–1508.
[66] E. Goncalves, R.F. Patella, Numerical study of cavitating flows with thermodynamic effect, Comput. Fluids 39 (2010) 99–113.
[67] B. Charriere, J. Decaix, E. Goncalves, A comparative study of cavitation models in a Venturi flow, Eur. J. Mech. B/Fluids 49 (2015) 287–297.
[68] C. Vortmann, G.H. Schnerr, S. Seeleck, Thermodynamic modelling and simulation of cavitating nozzle flow, Int. J. Heat Fluid Flow 24 (2003) 774–783.
[69] C.L. Merkle, J. Feng, P.E. Buelow, Computational modeling of the dynamics of sheet cavitation Vol. 2 (1998).
[70] R.F. Kunz, D.A. Boger, D.R. Stinebring, et al., A preconditioned Navier-Stokes method for two-phase flows with application to cavitation prediction, Comput. Fluids 29 (8) (2000) 849–875.

[71] I. Senocak, W. Shyy, Interfacial dynamics-based modelling of turbulent cavitating flows, Part I: Model development and steady-state computations, Int. J. Numer. Meth. Fluids 44 (9) (2004) 976–995.
[72] A. Hosangadi, V. Ahuja, Numerical study of cavitation cryogenic fluids, ASME J. Fluids Eng. 127 (2) (2005) 267–281.
[73] S. Shi, G. Wang, Numerical calculation of thermal effect on cavitation in cryogenic fluids, Chin. J. Mech. Eng. 25 (6) (2012) 1176–1183.
[74] T. Chen, B. Huang, G. Wang, et al., Effects of fluid thermophysical properties on cavitating flows, J. Mech. Sci. Technol. 29 (10) (2015) 4239–4246.
[75] T. Chen, G. Wang, B. Huang, et al., Numerical study of thermodynamic effects on liquid nitrogen cavitating flows, Cryogenics 70 (2015) 21–27.
[76] T.Z. Sun, Y.J. Wei, C. Wang, Computational analyses of cavitating flows in cryogenic liquid hydrogen, J. Harbin Inst. Technol. (New Ser.) 23 (5) (2016) 1–7.
[77] C.C. Tseng, W. Shyy, Modeling for isothermal and cryogenic cavitation, Int. J. Heat Mass Transf. 53 (1–3) (2010) 513–525.
[78] A. Hosangadi, V. Ahuja, R. Ungewitter, Analysis of thermal effects in cavitating liquid hydrogen inducers, J. Propul. Power 23 (6) (2007) 1225–1234.
[79] J.R. Maa, The role of interfaces in heat transfer processes, Adv. Colloid Interface Sci. 18 (1983) 227–280.
[80] S. Fujikawa, T. Akamatsu, Effects of the non-equilibrium condensation of vapour on the pressure wave produced by the collapse of a bubble in a liquid, J. Fluid Mech. 97 (3) (1980) 481–512.
[81] Y. Saito, R. Takami, I. Nakamori, et al., Numerical analysis of unsteady behavior of cloud cavitation around a NACA0015 foil, Comput. Mech. 40 (2007) 85–96.
[82] N. Ochiai, Y. Iga, M. Nohmi, et al., Numerical prediction of cavitation erosion intensity in cavitating flows around a Clark Y 11.7% hydrofoil, Journal of Fluid, Sci. Technol. 5 (3) (2010) 416–431.
[83] A. Gnanaskandan, K. Mahesh, A numerical method to simulate turbulent cavitating flows, Int. J. Multiph. Flow 70 (2015) 23–34.
[84] A.D. Le, J. Okajima, Y. Iga, Numerical simulation study of cavitation in liquefied hydrogen, Cryogenics 101 (2019) 29–35.
[85] S. Yang, C. Habchi, Real-fluid phase transition in cavitation modeling considering dissolved non-condensable gas, Phys. Fluids 32 (2020) 032102.
[86] S. Liu, S. Li, L. Zhang, et al., A mixture model with modified mass transfer expression for cavitating turbulent flow simulation, Eng. Comput. 25 (4) (2008) 290–304.
[87] A. Yu, Q. Tang, D. Zhou, et al., Entropy production analysis in two-phase cavitation flows with thermodynamic cavitation model, Appl. Therm. Eng. 171 (2020) 115099.
[88] A. Yu, Q. Tang, D. Zhou, Entropy production analysis in thermodynamic cavitating flow with the consideration of local compressibility, Int. J. Heat Mass Transf. 153 (2020) 119604.
[89] Schnerr G H and Sauer J, Physical and numerical modelling of unsteady cavitation dynamics, in: Proceedings of 4th International Conference on Multiphase Flow, New Orleans, USA, May 27-June 1, 2001.
[90] C.E. Brennen, Cavitation and Bubble Dynamics, Oxford University Press, Oxford, 1995, pp. 47–50.
[91] W. Yuan, J. Sauer, G.H. Schnerr, Modeling and computation of unsteady cavitation flows in injection nozzles, Mech. Industry 2 (5) (2001) 383–394.
[92] J. Zhu, Y. Chen, D. Zhao, et al., Extension of the Schnerr-Sauer model for cryogenic cavitation, Eur. J. Mech. B/Fluids 52 (2015) 1–10.
[93] J. Zhu, D. Zhao, L. Xu, et al., Interactions of vortices, thermal effects and cavitation in liquid hydrogen cavitating flows, Int. J. Hydrogen Energy 41 (2016) 614–631.
[94] X. Long, Q. Liu, B. Ji, et al., Numerical investigation of two typical cavitation shedding dynamics flow in liquid hydrogen with thermodynamic effects, Int. J. Heat Mass Transf. 109 (2017) 879–893.
[95] M.G. De Giorgi, A. Ficarella, D. Fontanarosa, Implementation and validation of an extended Schnerr-Sauer cavitation model for non-isothermal flows in OpenFOAM, Energy Procedia 126 (201709) (2017) 58–65.
[96] J. Zhu, S. Wang, L. Qiu, et al., Frequency characteristics of liquid hydrogen cavitating flow over a NACA0015 hydrofoil, Cryogenics 90 (2018) 7–19.
[97] Y. Liu, X. Li, W. Wang, et al., Numerical investigation on the evolution of forces and energy features in thermo-sensitive cavitating flow, Eur. J. Mech./B Fluids 84 (2020) 233–249.
[98] Kanfoud H, Lamloumi H and Zgolli R, A new model to simulate a cavitating flow, Proceedings of the International Renewable Energy Congress, November 5-7, 2010, Sousse, Tunisia, 310-314.
[99] F. Hong, J. Yuan, B. Zhou, Application of a new cavitation model for computations of unsteady turbulent cavitating flows around a hydrofoil, J. Mech. Sci. Technol. 31 (1) (2017) 249–260.
[100] F. Hong, W. Yu, F. Zhang, Numerical investigation of turbulent cavitating flow in an axial flow pump using a new transport-based model, J. Mech. Sci. Technol. 34 (2) (2020) 745–756.
[101] Plesset M S, Physical effects in cavitating flows, In: Fluid mechanics, acoustic and design of turbomachinery: Part I, NASA SP-304, edited by Lakshminarayana B, Britsch W R and Gearhart W S, 1974, 341-349.
[102] S.B. Martynov, D.J. Mason, M.R. Heikal, Numerical simulation of cavitation flows based on their hydrodynamic similarity, Int. J. Engine Res. 7 (2006) 283–296.
[103] A.K. Singhal, M.M. Athavale, H. Li, et al., Mathematical basis and validation of the full cavitation model, ASME J. Fluids Eng. 124 (3) (2002) 617–624.
[104] M.G. De Giorgi, D. Bello, A. Ficarella, Analysis of thermal effects in a cavitating orifice using Rayleigh equation and experiments, ASME J. Eng. Gas Turbines Power 132 (9) (2010) 092901.
[105] S. Tsuda, N. Tani, N. Yamanishi, Development and validation of a reduced critical radius model for cryogenic cavitation, ASME Journal of Fluids Engineering 134 (5) (2012) (10 pages).
[106] X.B. Zhang, Z. Wu, S.J. Xiang, et al., Modeling cavitating flow of cryogenic fluids with thermodynamic phase-change theory, Chin. Sci. Bull. 58 (4–5) (2013) 567–574.
[107] W.G. Zhao, L.X. Zhang, X.M. Shao, Numerical simulation of cavitation flow under high pressure and temperature, J. Hydrodyn. 23 (3) (2011) 289–294.
[108] X.B. Zhang, L.M. Qiu, H. Qi, et al., Modeling liquid hydrogen cavitating flow with the full cavitation model, Int. J. Hydrogen Energy 33 (2008) 7197–7206.
[109] Zwart P J, Gerber A G and Belamri T, A two-phase flow model for predicting cavitation dynamics, in: Proceedings of ICMF 2004 International Conference on Multiphase Flow, Yokohama, Japan, May 30-June 3, 2004.
[110] Y. Zhang, X.W. Luo, B. Ji, et al., A thermodynamic cavitation model for cavitating flow simulation in a wide range of water temperature, Chin. Phys. Lett. 27 (1) (2010) 016401.
[111] X.L. Tang, L.Y. Bian, F.J. Wang, et al., Numerical investigation on cavitating flows with thermodynamic effects in a diffuser-type centrifugal pump, J. Mech. Sci. Technol. 27 (6) (2013) 1655–1664.
[112] B. Huang, Q. Wu, G.Y. Wang, Numerical investigation of cavitating flow in liquid hydrogen, Int. J. Hydrogen Energy 39 (2014) 1698–1709.
[113] T.Z. Sun, X.F. Ma, Y.J. Wei, et al., Computational modeling of cavitating flows in liquid nitrogen by an extended transport-based cavitation model, Sci. China-Technol. Sci. 59 (2) (2015) 337–346.
[114] Y. Liu, X. Li, Z. Lin, et al., Numerical analysis of thermo-sensitive cavitating flows with special emphasises on flow separation and enstrophy conversion, Int. Commun. Heat Mass Transfer 125 (2021) 105336.
[115] S. Zhang, X. Li, Z. Zhu, Numerical simulation of cryogenic cavitating flow by an extended transport-based cavitation model with thermal effect, Cryogenics 92 (2018) 98–104.
[116] Li W, Yang Y, Shi W, et al, The correction and evaluation of cavitation model considering the thermodynamic effect, Mathematical Problems in Engineering, 2018, Volume 2018, https://doi.org/10.1155/2018/7217513.
[117] C. Shao, Z. Zhang, J. Zhou, Study of the flow in a cryogenic pump under different cavitation inducements by considering the thermodynamic effect, Int. J. Numer. Meth. Heat Fluid Flow 30 (9) (2020) 4307–4329.
[118] R. Xue, Y. Ruan, X. Liu, et al., The influence of cavitation on the flow characteristics of liquid nitrogen through spray nozzle: A CFD study, Cryogenics 86 (2017) 42–56.
[119] C. Wang, Y. Zhang, H. Hou, et al., Entropy production diagnostic analysis of energy consumption for cavitation flow in a two-stage LNG cryogenic submerged pump, Int. J. Heat Mass Transf. 129 (2019) 342–356.
[120] P. Song, J. Sun, Cryogenic cavitation mitigation in a liquid turbine expander of an air-separation unit through collaborative fine-tuned optimization of impeller and fairing cone geometries, Energies 13 (1) (2020) 50.
[121] B. Xu, J. Feng, F. Wan, et al., Numerical investigation of modified cavitation model with thermodynamic effect in water and liquid nitrogen, Cryogenics 106 (2020) 103049.
[122] Kinzel M P, Lindau J W and Kunz R F, A unified homogenous multiphase CFD model for cavitation, In: Proceedings of ASME 2017 Fluids Engineering Division Summer Meeting, July 30-August 3, 2017, Waikoloa, Hawaii, USA, 1-10.
[123] F.G. Hammitt, Effects of gas content upon cavitation inception, performance, and damage, J. Hydraul. Res. 10 (3) (1972) 259–290.
[124] E. Yilmaz, F.G. Hammitt, A. Keller, Cavitation inception thresholds in water and nuclei spectra by light-scattering technique, J. Acoust. Soc. Am. 59 (1976) 329–338.
[125] M.L. Billet, Cavitation nuclei measurements with an optical system, ASME J. Fluids Eng 108 (3) (1986) 366–372.
[126] T.J. O'Hern, L. d'Agostino, A.J. Acosta, Comparison of holographic and Coulter counter measurements of cavitation nuclei in the ocean, ASME J. Fluids Eng. 110 (2) (1988) 200–207.
[127] Z. Liu, C.E. Brennen, Cavitation nuclei Population and event rates, ASME J. Fluids Eng. 120 (4) (1998) 728–737.
[128] M.T. Khoo, J.A. Venning, B.W. Pearce, et al., Natural nuclei population dynamics in cavitation tunnels, Exp. Fluids 61 (2020), https://doi.org/10.1007/s00348-019-2843-x.
[129] S. Kumar, C.E. Brennen, Some nonlinear interactive effects in bubbly clouds, J. Fluid Mech. 253 (1993) 565–591.
[130] Y.C. Wang, Effects of nuclei size distribution on the dynamics of a spherical clod of cavitation bubbles, ASME J. Fluids Eng. 121 (4) (1999) 881–886.
[131] M. Blander, J.L. Katz, Bubble nucleation in liquids, AIChE J. 21 (5) (1975) 833–848.
[132] C.F. Delale, J. Hruby, F. Marsik, Homogeneous bubble nucleation in liquids: the classical theory revisited, J. Chem. Phys. 118 (2) (2003) 792–806.
[133] M. Blander, Bubble nucleation in liquids, Adv. Colloid Interface Sci. 10 (1979) 1–32.
[134] B. Wyslouzil, J. Wölk, Overview: Homogeneous nucleation from the vapor phase-the experimental science, J. Chem. Phys. 145 (2016) 2117021.
[135] T. Kinjo, M. Matsumoto, Cavitation processes and negative pressure, Fluid Phase Equilib. 144 (1998) 343–350.
[136] H.Y. Kwak, R.L. Panton, Tensile strength of simple liquids predicted by a model of molecular interactions, J. Phys. D Appl. Phys. 18 (1985) 647–659.
[137] H.Y. Kwak, S.D. Oh, Gas–vapor bubble nucleation—a unified approach, J. Colloid Interface Sci. 278 (2004) 436–446.
[138] H.Y. Kwak, Vapor bubble nucleation: a microscopic phenomenon, KSME Int. J. 18 (8) (2004) 1271–1287.

[139] K.T. Byun, H.Y. Kwak, A model of laser-induced cavitation, Jpn. J. Appl. Phys. 43 (2) (2004) 621–630.
[140] F. Takemura, Y. Matsumoto, Influence of internal phenomena on gas bubble motion, JSME Int. J., Ser. B 37 (4) (1994) 736–745.
[141] Y. Ito, H. Wakamatsu, T. Nagasaki, Numerical simulation of sub-cooled cavitating flow by using bubble size distribution, J. Therm. Sci. 12 (4) (2003) 350–356.
[142] Y. Ito, Numerical model and validation for cryogenic high-speed cavitating flow based on bubble size distribution model in consideration of rigorous heat transfer around bubble oscillation, J. Japan Soc. Aeronaut. Space Sci. 56 (657) (2008) 456–463.
[143] Y. Ito, X. Zheng, T. Nagasaki, Numerical simulation using the bubble size distribution model of cryogenic cavitation around an axial inducer, in: Proceedings of 29th IAHR Symposium on Hydraulic Machinery and Systems, 2019, https://doi.org/10.1088/1755-1315/240/6/062015.
[144] C.F. Delale, K. Okita, Y. Matsumoto, Steady-state cavitating nozzle flows with nucleation, ASME J. Fluids Eng. 127 (4) (2005) 770–777.
[145] D. Li, S. Liu, Y. Wei, et al., A turbulent two-phase model for predicting cavitating flow based on homogenous nucleation theory, Int. Commun. Heat Mass Transfer 97 (2018) 17–29.
[146] Z.H. Ban, K.K. Lau, A.M. Sharif, Prediction of the bubble nucleation rate in a quasistable cavitating nozzle using 2D computational fluid dynamics and enhanced classical nucleation theory, Eng. Applications Comput. Fluid Mech. 9 (1) (2015) 247–258.
[147] M.G. De Giorgi, A. Ficarella, D. Fontanarosa, Numerical Investigation of nonisothermal cavitating flows on hydrofoils by means of an extended Schnerr-Sauer model coupled with a nucleation model, ASME J. Eng. Gas Turbines Power 142 (2020) 041003.
[148] M.G. De Giorgi, D. Fontanarosa, A. Ficarella, Characterization of unsteady cavitating flow regimes around a hydrofoil, based on an extended Schnerr-Sauer model coupled with a nucleation model, Int. J. Multiph. Flow 115 (2019) 158–180.
[149] Y. Kodama, N. Take, S. Tamiya, et al., The effect of nuclei on the inception of bubble and sheet cavitation on axisymmetric bodies, ASME J. Fluids Eng. 103 (4) (1981) 557–563.
[150] R.S. Meyer, M.L. Billet, J.W. Holl, Freestream nuclei and traveling bubble-cavitation, ASME J. Fluids Eng. 114 (4) (1992) 672–679.
[151] C.T. Hsiao, G.L. Chahine, H.L. Liu, Scaling effect on prediction of cavitation inception in a line vortex flow, ASME J. Fluids Eng. 125 (1) (2003) 53–60.
[152] G.F. Oweis, I.E. van der Hout, C. Iyer, et al., Capture and inception of bubbles near line vortices, Phys. Fluids 17 (2005) 022105.
[153] M.R. Maxey, J.J. Riley, Equations of motion for a small rigid sphere in a nonuniform flow, Phys. Fluids 26 (1983) 883–889.
[154] C.T. Hsiao, L.L. Pauley, Study of tip vortex cavitation inception using Navier-Stokes computation and bubble dynamics model, ASME J. Fluids Eng. 121 (1) (1999) 198–204.
[155] K.J. Farrell, Eulerian/Lagrangian analysis for the prediction of cavitation inception, ASME J. Fluids Eng. 125 (1) (2003) 46–52.
[156] C.T. Hsiao, G.L. Chahine, Prediction of tip vortex cavitation inception using coupled spherical and nonspherical bubble models and Navier-Stokes computations, J. Mar. Sci. Technol. 8 (2004) 99–108.
[157] C.T. Hsiao, G.L. Chahine, Scaling of tip vortex cavitation inception noise with a bubble dynamics model accounting for nuclei size distribution, ASME J. Fluids Eng. 127 (1) (2005) 55–65.
[158] J.R. Blake, Cavitation bubbles near boundaries, Annu. Rev. Fluid Mech. 19 (1987) 99–123.
[159] K. Okuda, T. Ikohagi, Numerical simulation of collapsing behavior od bubble clouds, JSME Trans.-Ser. B 62 (603) (1996) 38–43.
[160] Y. Matsumoto, S. Yoshizawa, Behaviour of a bubble cluster in an ultrasound field, Int. J. Numer. Meth. Fluids 47 (2005) 591–601.
[161] N. Ochiai, J. Ishimoto, Numerical investigation of multi-bubble behavior and induced pressure in a megasonic field, J. Fluid Mech. 818 (2017) 562–594.
[162] N. Ochiai, J. Ishimoto, Numerical analysis of the effect of bubble distribution on multiple-bubble behavior, Ultrason.-Sonochem. 61 (2020) 104818.
[163] E. Johnsen, T. Colonius, Shock-induced collapse of a gas bubble in shockwave lithotripsy, J. Acoust. Soc. Am. 124 (4) (2008) 2011–2020.
[164] E. Johnsen, T. Colonius, Numerical simulations of non-spherical bubble collapse, J. Fluid Mech. 629 (2009) 231–262.
[165] D. Fuster, A review of models for bubble clusters in cavitating flow, Flow, Turbulence Combust. 102 (2019) 497–536.
[166] M. Nohmi, T. Ikohagi, Y. Iga, Numerical prediction method of cavitation erosion, Proceedings of 2008 ASME Fluids Engineering Conference August 10–14, Jacksonville, Florida USA, 2008.
[167] N. Ochiai, Y. Iga, M. Nohmi, et al., Study of quantitative numerical prediction of cavitation erosion in cavitating flow, ASME J. Fluids Eng. 135 (2013) 011303.
[168] Y. Tomita, A. Shima, On the behavior of a spherical bubble and the impulse pressure in a viscous compressible liquid, Bull. JSME 20 (19) (1977) 1453–1460.
[169] M. Khojasteh-Manesh, M. Mahdi, Evaluation of cavitation erosion intensity in a microscale nozzle using Eulerian-Lagrangian Bubble Dynamic Simulation, ASME J. Fluids Eng. 141 (2019) 061303.
[170] J.B. Keller, I.I. Kolodner, Damping of underwater explosion bubble oscillations, Phys. Fluids 27 (10) (1956) 1152–1161.
[171] A. Kubota, H. Kato, H. Yamaguchi, A new modelling of cavitating flows: A numerical study of unsteady cavitation on a hydrofoil section, J. Fluid Mech. 240 (1992) 59–96.
[172] J. Ishimoto, K. Kamijo, Numerical simulation of cavitating flow of liquid helium in Venturi channel, Cryogenics 43 (2003) 9–17.
[173] E. Giannadakis, M. Gavaises, C. Arcoumanis, Modelling of cavitation in diesel injector nozzles, J. Fluid Mech. 616 (2008) 153–193.
[174] M. Abdel-Maksoud, D. Hanel, U. Lantermann, Modeling and computation of cavitation in vortical flow, Int. J. Heat Fluid Flow 31 (2010) 1065–1074.
[175] J. Ma, C.T. Hsiao, G.L. Chahine, Euler-Lagrange simulations of bubble cloud dynamics near a wall, ASME J. Fluids Eng. 137 (2015) 041301.
[176] C.T. Hsiao, J. Ma, G.L. Chahine, Multiscale two-phase flow modelling of sheet and cloud cavitation, Int. J. Multiph. Flow 90 (2017) 102–117.
[177] Hammerl G and Wall W A, A four-way coupled Euler–Lagrange approach using a ariational multiscale method for simulating cavitation, in: 9th International Symposium on Cavitation (CAV2015), Journal of Physics: Conference Series 656, 2015, 012125.
[178] J. Ma, C.T. Hsiao, G.L. Chahine, A physics based multiscale modelling of cavitating flows, Comput. Fluids 145 (2017) 68–84.
[179] L. Li, Z. Wang, X. Li, Z. Zhu, Multiscale modeling of tip-leakage cavitating flows by a combined volume of fluid and discrete bubble model, Phys. Fluids 33 (2021) 062104.
[180] A. Peters, O. el Moctar, Numerical assessment of cavitation-induced erosion using multi-scale Euler-Lagrange method, J. Fluids Mech. 894 (2020) A19.
[181] M.S. Plesset, S.A. Zwick, The growth of vapor bubbles in superheated liquids, J. Appl. Phys. 25 (4) (1954) 493–500.
[182] S.A. Zwick, M.S. Plesset, On the dynamics of small vapor bubbles in liquids, J. Math. Phys. 33 (1–4) (1954) 308–330.
[183] G. Birkhoff, R.S. Margulies, W.A. Horning, Spherical Bubble Growth, Phys. Fluids 1 (1958) 201–204.
[184] L.E. Scriven, On the dynamics of phase growth, Chem. Eng. Sci. 10 (1959) 1–13.
[185] S.A. Zwick, Growth of vapor bubbles in a rapidly heated liquid, Phys. Fluids 3 (5) (1960) 685–692.
[186] N. Zuber, The dynamics of vapor bubbles in nonuniform temperature fields, Int. J. Heat Mass Transf. 2 (1961) 83–98.
[187] S.G. Bankoff, Asymptotic growth of a bubble in a liquid with uniform initial superheat, Appl. Sci. Res.-Sect. A 12 (1964) 267–281.
[188] B.B. Mikic, W.M. Rohsenow, P. Griffith, On bubble growth rates, Int. J. Heat Mass Transfer 13 (1970) 657–666.
[189] S.J. Board, R.B. Duffey, Spherical vapour bubble growth in superheated liquids, Chem. Eng. Sci. 26 (1971) 263–274.
[190] H.K. Forster, N. Zuber, Dynamics of vapor bubbles and boiling heat transfer, AIChE J. 1 (4) (1971) 531–535.
[191] T.G. Theofanous, P.D. Patel, Universal relations for bubble growth, Int. J. Heat Mass Transf. 19 (1976) 425–429.
[192] M.S. Plesset, A. Prosperetti, Vapour-bubble growth in a superheated liquid, J. Fluid Mech. 85 (1978) 349–368.
[193] M.S. Plesset, A. Prosperetti, Bubble dynamics and cavitation, Annu. Rev. Fluid Mech. 9 (1977) 145–185.
[194] H.S. Lee, H. Merte, Spherical vapor bubble growth in uniformly superheated liquids, Int. J. Heat Mass Transf. 39 (12) (1996) 2427–2447.
[195] A.J. Robinson, R.L. Judd, The dynamics of spherical bubble growth, Int. J. Heat Mass Transf. 47 (2004) 5101–5113.
[196] S.A. Mohammadein, S.A. Gouda, Temperature distribution in a mixture surrounding a growing vapour bubble, Heat Mass Transfer 42 (2006) 359–363.
[197] J. Bhati, S. Paruya, A semi-analytical method for computing the dynamics of bubble growth: The effect of superheat and operating pressure, Ind. Eng. Chem. Res. 57 (2018) 15159–15171.
[198] J. Franc, C. Pellone, Analysis of thermal effects in a cavitating inducer using Rayleigh equation, ASME J. Fluids Eng. 129 (8) (2007) 974–983.
[199] D. Colombet, E. Goncalvès Da Silva, R. Fortes-Patella, On numerical simulation of cavitating flows under thermal regime, Int. J. Heat Mass Transf. 105 (2017) 411–428.
[200] M.G. Rodio, M.G. De Giorgi, A. Ficarella, Influence of convective heat transfer modeling on the estimation of thermal effects in cryogenic cavitating flows, Int. J. Heat Mass Transf. 55 (2012) 6538–6554.
[201] De Giorgi M G, Ficarella A, Chiara F, et al, Experimental and Numerical Investigations of Cavitating Flows, AIAA 2005-5278, 35th AIAA Fluid Dynamics Conference and Exhibit 6-9 June 2005, Toronto, Ontario Canada.
[202] A. Yu, X.W. Luo, B. Ji, et al., Cavitation simulation with consideration of the viscous effect at large liquid temperature variation, Chin. Phys. Lett. 31 (8) (2014) 086401.
[203] K. Pang, Y. Li, W. Yang, et al., A calculation model considering thermodynamic and viscosity effects, Eng. Comput. 35 (11) (2018) 2308–2326.
[204] B. Huang, Y.L. Young, G. Wang, et al., Combined experimental and computational investigation of unsteady structure of sheet/cloud cavitation, ASME J. Fluids Eng. 135 (2013) 071301.
[205] Y. Zhao, G. Wang, B. Huang, A cavitation model for computations of unsteady cavitating flows, Acta Mech. Sin. 32 (2) (2016) 273–283.
[206] R. Mettin, I. Akhatov, U. Parlitz, et al., Bjerknes forces between small cavitation bubbles in a strong acoustic field, Phys. Rev. E 56 (3) (1997) 2924–2931.
[207] M. Ida, A characteristic frequency of two mutually interacting gas bubbles in an acoustic field, Phys. Lett. A 297 (2002) 210–217.
[208] M. Ida, Alternative interpretation of the sign reversal of secondary Bjerknes force acting between two pulsating gas bubbles, Phys. Rev. E 67 (2003) 056617.
[209] G.L. Chahine, Pressures generation by bubble cloud collapse, Chem. Eng. Commun. 28 (4–6) (1984) 353–367.
[210] Takahira H, Akamatsu T and Fujikawa S, Dynamics of a cluster of bubbles in a liquid (theoretical analysis), JSME Int. J. 37(2), 297–305.
[211] A. Biesheuvel, L. van Wijngaarden, Two-phase flow equations for a dilute dispersion of gas bubbles in liquid, J. Fluid Mech. 148 (1984) 301–318.

[212] U. Rasthofer, F. Wermedlinger, P. Hadijfoukas, et al., Large scale simulation of cloud cavitation collapse, Procedia Comput. Sci. 108C (2017) 1763–1772.
[213] Y. Ye, G. Li, Modeling of hydrodynamic cavitating flows considering the bubble-bubble interaction, Int. J. Multiphase Flows 84 (2016) 155–164.
[214] Y. Ye, X. Zhu, F. Lai, et al., Application of the semi-analysis cavitation model to flows in a centrifugal pump, Int. Commun. Heat Mass Transfer 86 (2017) 92–100.
[215] V.A. Sosinovich, V.A. Tsyganov, B.A. Kolovandin, et al., Model of gas bubble breakup in a turbulent liquid flow, J. Eng. Phys. Thermodyn. 68 (2) (1995) 164–175.
[216] T. Du, Y. Wang, L. Liao, et al., A numerical model for the evolution of internal structure of cavitation cloud, Phys. Fluids 28 (2016) 077103.
[217] T. Du, Y. Wang, C. Huang, et al., A numerical model for cloud cavitation based on bubble cluster, Theor. Appl. Mech. Lett. 7 (2017) 231–234.
[218] M.A. Maiga, O. Coutier-Delgosha, D. Buisine, A new cavitation model based on bubble-bubble interactions, Phys. Fluids 30 (2018) 12330.
[219] D.D. Jospeh, Cavitation in a flowing liquid, Phys. Rev. E 51 (3) (1995) R1649–R1650.
[220] A. Asnaghi, A. Feymark, R.E. Bensow, Improvement of cavitation mass transfer modelling based on local flow properties, Int. J. Multiph. Flow 93 (2017) 142–157.
[221] F. Hong, Z. Gao, L. Liu, et al., Numerical investigation of the turbulent cavitating flow over submerged bodies, Int. J. Fluid Mach. Syst. 11 (1) (2018) 85–96.
[222] J. Dumond, F. Magagnato, A. Class, Stochastic-field cavitation model, Phys. Fluids 25 (2013) 073302.
[223] L. Valino, A field Monte Carlo formulation for calculating the probability density function of a single scalar in a turbulent flow, Flow Turbulence Combust. 60 (2) (1998) 157–172.
[224] M. Morgut, E. Nobile, I. Bilus, Comparison of mass transfer models for the numerical prediction of sheet cavitation around a hydrofoil, Int. J. Multiph. Flow 37 (2011) 620–626.
[225] W. Jin, X. Xu, Y. Tang, et al., Coefficient adaptation method for the Zwart model, J. Appl. Fluid Mech. 11 (6) (2018) 1665–1678.
[226] H. Zhou, M. Xiang, P.N. Okolo, et al., An efficient calibration approach for cavitation model constants based on OpenFOAM platform, J. Mar. Sci. Technol. 24 (2019) 1043–1056.
[227] A. Sikirica, Z. Carija, I. Lucin, et al., Cavitation model calibration using machine learning assisted workflow, Mathematics 2020 (2017) 8, https://doi.org/10.3390/math8122107.
[228] G.A. Pinhasi, A. Ullmann, A. Dayan, Modeling of flashing two-phase flow, Rev. Chem. Eng. 21 (3–4) (2005) 133–261.
[229] K. Ishikawa, Y. Umemura, T. Himeno, et al., Numerical analysis on unsteady cavitation by direct interface tracking approach, Trans. Japan Soc. Aeronaut. Space Sci. 12 (29) (2014) 63–69.
[230] S.W. Welch, J. Wilson, A volume of fluid based method for fluid flows with phase change, J. Comput. Phys. 160 (2000) 662–682.
[231] V.K. Dhir, Numerical simulations of pool-boiling heat transfer, AIChE J. 47 (4) (2001) 813–834.
[232] P. Zima, F. Marsik, M. Sedlar, Cavitation rates in water with dissolved gas and other impurities, J. Therm. Sci. 12 (2) (2003) 151–156.
[233] Farajisarir D, Growth and collapse of vapour bubbles in convective subcooled boiling of water, MSc Thesis, 1993, University of British Columbia, Canada.
[234] D. Sarker, W. Ding, U. Hampel, Bubble growth during subcooled nucleate boiling on a vertical heater: A mechanistic attempt to evaluate the role of surface characteristics on microlayer evaporation, Appl. Therm. Eng. 153 (2019) 565–574.
[235] Gelder T F, Ruggeri R S and Moore R D, Cavitation similarity considerations based on measured pressure and temperature depressions in cavitated regions of Freon 114, NASA TN D-3509, 1966.
[236] B. Ji, X.W. Luo, X.F. Peng, et al., Numerical investigation of the ventilated cavitating flow around an under-water vehicle based on a three-component cavitation model, J. Hydrodyn. 22 (6) (2010) 753–759.
[237] F. Hong, Z. Guo, L. Liu, et al., Numerical investigation of the turbulent cavitating flow over submerged bodies, Int. J. Fluid Mach. Syst. 11 (1) (2018) 85–96.
[238] F. Giussani, F. Fiscaglia, G. Saez-Mischlich, et al., A three-phase VOF solver for the simulation of in-nozzle cavitation effects on liquid atomization, J. Comput. Phys. 406 (2020) 109068.
[239] M.P. Kinzel, J.W. Lindau, R.F. Kinz, An assessment of computational fluid dynamics cavitation models using bubble growth theory and bubble transport modelling, ASME J. Fluids Eng. 141 (2019) 041301.
[240] M. Xu, H. Cheng, B. Ji, et al., LES of tip-leakage cavitating flow with special emphasis on different tip clearance sizes by a new-Euler-Lagrangian cavitation model, Ocean Eng. 213 (2020) 107661.
[241] W.G. Li, Modelling viscous oil cavitating flow in a centrifugal pump, ASME J. Fluids Eng. 138 (1) (2016) 011303.
[242] R. Mishra, D. Jiwani, D. Jarrahbashi, Three-component multi-fluid modeling of pseudo-cavitation phenomenon in diesel injector nozzles, Int. J. Engine Res. (2021), https://doi.org/10.1177/1468087421993348.
[243] A. Iannatti, M.T. Stickland, W.M. Dempster, An advanced CFD model to study the effect non-condensable gas on cavitation in positive displacement pumps, Open Eng. 5 (2015) 323–331.
[244] G. Wang, M. Ostoja-Starzewski, Large eddy simulation of a sheet/cloud cavitation on a NACA0015 hydrofoil, Appl. Math. Model. 31 (2007) 417–447.
[245] R.E. Bensow, G. Bark, Implicit LES predictions of the cavitating flow on a propeller, ASME J. Fluids Eng. 132 (2010) 041302.
[246] E. Roohi, A.P. Zahiri, M. Passandideh-Fard, Numerical simulation of cavitation around a two-dimensional hydrofoil using VOF method and LES turbulence model, Appl. Math. Model. 37 (2013) 6469–6488.
[247] N.X. Lu, R.E. Bensow, G. Bark, Large eddy simulation of cavitation development on highly skewed propellers, J. Mar. Sci. Technol. 19 (2014) 197–214.
[248] A. Gnanaskandan, K. Mahesh, Large eddy simulation of the transition from sheet to cloud cavitation over a wedge, Int. J. Multiph. Flow 83 (2016) 86–102.
[249] A. Asnaghi, U. Svennberg, R.E. Bensow, Large eddy simulations of cavitating tip vortex flows, Ocean Eng. 195 (2020) 106703.